

# KECK SPECTROSCOPY OF $3 < Z < 7$ FAINT LYMAN BREAK GALAXIES: THE IMPORTANCE OF NEBULAR EMISSION IN UNDERSTANDING THE SPECIFIC STAR FORMATION RATE AND STELLAR MASS DENSITY

DANIEL P. STARK<sup>1,2</sup>, MATTHEW A. SCHENKER<sup>3</sup>, RICHARD ELLIS<sup>3</sup>, BRANT ROBERTSON<sup>1</sup>, ROSS MCLURE<sup>4</sup>, JAMES DUNLOP<sup>4</sup>

*Draft version July 27, 2018*

## ABSTRACT

The physical properties inferred from the spectral energy distributions of  $z > 3$  galaxies have been influential in shaping our understanding of early galaxy formation and the role galaxies may play in cosmic reionization. Of particular importance is the stellar mass density at early times which represents the integral of earlier star formation. An important puzzle arising from the measurements so far reported is that the specific star formation rates (sSFR) evolve far less rapidly than expected in most theoretical models. Yet the observations underpinning these results remain very uncertain, owing in part to the possible contamination of rest-optical broadband light from strong nebular emission lines. To quantify the contribution of nebular emission to broad-band fluxes, we investigate the spectral energy distributions of 92 spectroscopically-confirmed galaxies in the redshift range  $3.8 < z < 5.0$  chosen because the H $\alpha$  line lies within the *Spitzer*/IRAC  $3.6\mu\text{m}$  filter. We demonstrate that the  $3.6\mu\text{m}$  flux is systematically in excess of that expected from stellar continuum alone, which we derive by fitting the SED with population synthesis models. No such excess is seen in a control sample of spectroscopically-confirmed galaxies with  $3.1 < z < 3.6$  in which there is no nebular contamination in the IRAC filters. From the distribution of our  $3.6\mu\text{m}$  flux excesses, we derive an H $\alpha$  equivalent width distribution and consider the implications both for the derived stellar masses and the sSFR evolution. The mean rest-frame H $\alpha$  equivalent width we infer at  $3.8 < z < 5.0$  (270 Å) indicates that nebular emission contributes at least 30% of the  $3.6\mu\text{m}$  flux and, by implication, nebular emission is likely to have a much greater impact for galaxies with  $z \simeq 6 - 7$  where both warm IRAC filters are contaminated. Via our empirically-derived equivalent width distribution we correct the available stellar mass densities and show that the sSFR evolves more rapidly at  $z > 4$  than previously thought, supporting up to a  $5\times$  increase between  $z \simeq 2$  and 7. Such a trend is much closer to theoretical expectations. Given our findings, we discuss the prospects for verifying quantitatively the nebular emission line strengths prior to the launch of the James Webb Space Telescope.

*Subject headings:* galaxies: formation – galaxies: evolution – galaxies: starburst – galaxies: high redshift – ultraviolet: galaxies – surveys

## 1. INTRODUCTION

Through detailed photometry of Lyman break galaxies (LBGs) undertaken with the Hubble and Spitzer Space Telescopes, much has been learned regarding the physical properties of galaxies beyond a redshift  $z \simeq 3$ . Stellar masses and star formation rates have now been inferred from broadband photometric spectral energy distributions (SEDs) for thousands of galaxies spanning the redshift range  $3 < z < 7$  (e.g., Egami et al. 2005; Eyles et al. 2005; Labbé et al. 2006; Eyles et al. 2007; Stark et al. 2007, 2009; Ono et al. 2010; González et al. 2010; Labbé et al. 2010a,b; González et al. 2011a; Lee et al. 2012; Reddy et al. 2012b; Curtis-Lake et al. 2012). The stellar mass density derived from these studies has proven a useful integrated constraint on the contribution of galaxies to reionization (e.g., Robertson et al. 2010), while the evolution of physical properties has provided insight into the processes which govern the assembly of

early galaxies (e.g., Finlator et al. 2011; Davé et al. 2011, 2012).

A potentially significant puzzle has recently emerged from these studies through measurement of the specific star formation rate (sSFR) at  $z > 2$ . Current observations demonstrate that between  $z \simeq 2$  and  $z \simeq 7$ , the sSFR in galaxies of fixed stellar mass does not evolve strongly (e.g., Stark et al. 2009; González et al. 2010), with recent estimates indicating at most a factor of two increase between  $z \simeq 2$  and 7 (e.g., Bouwens et al. 2012b; Reddy et al. 2012b). This is in contrast to simple expectations from semi-analytic models and numerical simulations (e.g., Weinmann et al. 2011; Davé et al. 2011, 2012) which predict that the sSFR should closely match the inflow rate of baryonic material. As this mass inflow rate is thought to increase with redshift as  $\dot{M}/M \simeq (1+z)^{2.25}$  (Neistein & Dekel 2008; Dekel et al. 2009), we should expect nearly a  $10\times$  increase in sSFR in galaxies of fixed stellar mass over  $2 < z < 7$ , in marked contrast to the observations.

The physical cause of the discrepancy associated with the sSFR evolution remains unclear. As discussed previously (e.g., Bouché et al. 2010; Dutton et al. 2010; Weinmann et al. 2011; Davé et al. 2011, 2012; Reddy et al. 2012b), a plateau in the redshift dependence of the sSFR would suggest star formation is more

<sup>1</sup> Department of Astronomy, Steward Observatory, University of Arizona, 933 North Cherry Avenue, Rm N204, Tucson, AZ, 85721, dpstark@email.arizona.edu

<sup>2</sup> Hubble Fellow

<sup>3</sup> Cahill Center of Astronomy & Astrophysics, California Institute of Technology, MS 249-17, Pasadena, CA 91125

<sup>4</sup> Institute for Astronomy, University of Edinburgh, Royal Observatory, Edinburgh, EH9 3HJ

inefficient at  $z > 6$  than at  $z \simeq 2$ . Various physical processes might be invoked to impede star formation, such as the inefficient formation of molecular hydrogen in low metallicity galaxies (e.g., Robertson & Kravtsov 2008; Gnedin et al. 2009; Krumholz & Dekel 2012) or an increase in the efficiency with which cold gas is removed via large-scale outflows.

Irrespective of any mechanism that might inhibit star formation at early times, it is difficult to reconcile such an inefficiency with the notion that early galaxies provide the ionizing photons responsible for reionization (Robertson et al. 2010). For example, the steep faint end slope of the ultraviolet luminosity function (UV LF) at  $z > 6$  (Bouwens et al. 2011) implies that star formation in low mass dark matter halos becomes *more efficient* at earlier times (e.g., Trenti et al. 2010), in contrast to the implications of the sSFR measurements.

Given these difficulties, it is prudent that we reconsider the accuracy of the data that is used to infer the sSFR and its evolution. The two basic ingredients are the star formation rates and the stellar masses. The  $z > 4$  measurements have indeed changed since the original articles (e.g., Stark et al. 2009; González et al. 2010), mostly as a result of improved dust corrections following improved near-infrared photometry (e.g., Bouwens et al. 2012b). The new dust corrections have served to increase the  $z \simeq 4$  sSFR measurements by a factor  $\simeq 2$ . However, since negligible extinction is inferred at  $z \simeq 6 - 7$ , the sSFR still remains constant over  $4 < z < 7$  (Bouwens et al. 2012b) although a factor of 2 higher than at  $z \simeq 2 - 3$  (Reddy et al. 2012b).

A potentially more important problem is the possible contribution of rest-frame optical nebular emission lines (e.g., [O II], [O III], H $\alpha$ ) to the broad-band fluxes used to infer the stellar masses. Such emission lines, could significantly affect the inferred amplitude of a Balmer Break, leading to an overestimate of the stellar mass and thereby an underestimate of the sSFR. Figure 1 illustrates how the various nebular emission lines contaminate the key photometric filters as a function of redshift. Beyond  $z \simeq 4$ , the key filters of interest in the determination of stellar masses are the *Spitzer*/IRAC warm bands at  $3.6\mu\text{m}$  and  $4.5\mu\text{m}$ . It is particularly striking that, at  $z \gtrsim 5$ , the strongest rest-frame optical nebular lines ([OIII] $\lambda 5007$  and H $\alpha$ ) contaminate both *Spitzer*/IRAC filters. Although many  $z \gtrsim 5$  galaxies are detected with *Spitzer* (e.g., Egami et al. 2005; Eyles et al. 2005; Stark et al. 2009; Labbé et al. 2010a,b; González et al. 2010, 2011a; Richard et al. 2011b), contamination by nebular emission could significantly affect the interpretation of their SEDs.

Accounting for nebular emission in the SEDs of high redshift galaxies has been considered by several earlier works (e.g., Schaerer & de Barros 2009, 2010; Ono et al. 2010; de Barros et al. 2012). In general terms, their approach has been to use ‘forward modeling’ techniques based on adding nebular emission contributions to stellar population synthesis models in order to demonstrate the possible implications of its inclusion. However, such ‘nebular+stellar’ model fits cannot provide a precise unambiguous measure of nebular contamination for several reasons. Firstly, there are numerous uncertainties in how the contribution of nebular emission should be added.

These include the nebular extinction law and ionizing photon escape fraction. Secondly, for galaxies at  $z > 5$ , for which there is no uncontaminated measure of the stellar continuum (Figure 1), the uncertainties are particularly large. Finally, and perhaps most importantly, without a spectroscopic redshift, addressing both the nebular contamination and the photometric redshift of the galaxy from the same photometric data leads to great uncertainties; there is no *a priori* indication of which photometric bands are contaminated by nebular emission.

Fortunately, by virtue of our deep Keck spectroscopic survey (Stark et al. 2010, Stark et al. 2011, Jones et al. 2012, Schenker et al. 2012) and our nebular+stellar population synthesis code (Robertson et al. 2010), we can use the availability of HST-*Spitzer* SEDs to make progress in addressing this issue. While the question of contamination by nebular emission at  $z > 5$  must await the infrared spectroscopic capabilities of James Webb Space Telescope, we can test our spectroscopic range  $3.8 < z < 5.0$  for contamination by H $\alpha$  in the *Spitzer*/IRAC  $3.6\mu\text{m}$  broadband filter. Our approach follows that of Shim et al. (2011) who demonstrated that galaxies in this redshift window are typically significantly brighter at  $3.6\mu\text{m}$  than at  $4.5\mu\text{m}$ . By comparing their flux density at  $3.6\mu\text{m}$  to that expected from stellar continuum alone, Shim et al. (2011) argued that many galaxies at  $z > 4$  show evidence for strong H $\alpha$  emission, with typical EWs significantly greater than those seen at  $z \simeq 2$ .

Here we seek to apply a similar technique to our spectroscopic sample (Stark et al. 2010, 2011) with the goal of estimating the *distribution of H $\alpha$  equivalent widths* present in galaxies at  $3.8 < z < 5.0$ . Equipped with this external constraint on the strength of nebular emission, we can then determine how stellar masses and the sSFR of  $z > 4$  galaxies are likely to be altered by emission line contamination. In particular, we will explore whether our estimated degree of nebular contamination could be sufficient at the highest redshifts to permit a rapid rise in the redshift-dependent sSFR as expected from theoretical models.

The present paper is organized as follows. In §2, we discuss the selection of the spectroscopic sample used in our analysis. In §3, we introduce the details of our SED fitting procedure used to estimate the strength of nebular emission lines in the various filters. In §4 we use our spectroscopic sample to estimate the equivalent width distribution of H $\alpha$  in the redshift range  $3.8 < z < 5.0$  and then use these measurements to assess the impact of nebular emission on the derived stellar masses and star formation rates of  $z > 4$  galaxies. In §5, we discuss the impact that our findings have for the evolution in the integrated stellar mass density and specific star formation rates of galaxies at  $z > 4$ .

Throughout this paper we adopt a  $\Lambda$ -dominated, flat universe with  $\Omega_\Lambda = 0.7$ ,  $\Omega_M = 0.3$  and  $H_0 = 70 h_{70} \text{km s}^{-1} \text{Mpc}^{-1}$ . All magnitudes are quoted in the AB system (Oke & Gunn 1983).

## 2. DATA

In this paper, we will focus our analysis on the interpretation of broad-band spectral energy distributions for a  $z > 3$  sample with known spectroscopic redshifts. The spectroscopic sample is drawn from earlier papers

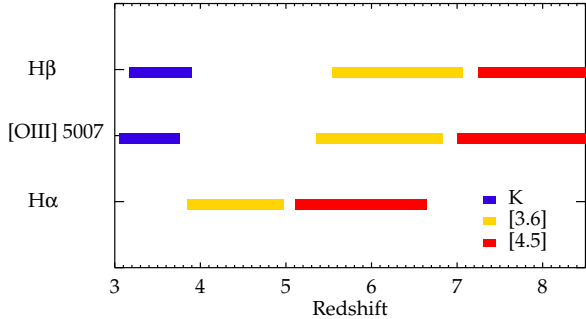


FIG. 1.— Emission line contamination of broadband photometry. Colored stripes denote redshift ranges over which emission lines contaminate the  $K_s$ -band (dark blue), IRAC  $3.6\ \mu\text{m}$  (yellow), and IRAC  $4.5\ \mu\text{m}$  (red).  $H\alpha$  emission is expected in the  $3.6\ \mu\text{m}$  filter at  $3.8 < z < 5.0$ . Note that at  $5 \lesssim z \lesssim 7$ , both IRAC filters used for measuring stellar masses are contaminated by emission lines. Beyond  $z \simeq 7$ , only the  $4.5\ \mu\text{m}$  filter is contaminated by strong nebular emission.

(Stark et al. 2010, 2011). Full details can be found in these articles, but we offer the reader a brief summary here. Spectroscopy of  $z > 3$  LBGs in the two GOODS fields was undertaken at the Keck Observatory using the DEIMOS spectrograph (Faber et al. 2003). As discussed in Stark et al. (2010), LBGs were selected using standard ‘dropout’ criteria (e.g., Bouwens et al. 2007; Stark et al. 2009) to a limiting magnitude of  $z_{850} \simeq 27$  using the GOODS v2 public photometric catalogs (e.g., Giavalisco et al. 2004). Taking advantage of a similar spectroscopic campaign undertaken using the FORS2 in GOODS-South (e.g., Vanzella et al. 2009), we retrospectively constructed a VLT sample using the same photometric criteria. The combined Keck plus VLT survey comprises 157 galaxies in the redshift range  $3.8 < z < 5.0$  which satisfy the dropout criteria. As we will discuss below, only a subset of these will be used in our analysis.

A key requirement for the derivation of stellar masses and specific star formation rate is precise broad band photometry from which SEDs for galaxies of known spectroscopic redshifts can be determined. In GOODS-South, we use the public release of the Wide Field Camera 3 (WFC3) imaging from the CANDELS Multi-Cycle Treasury Program (Grogin et al. 2011; Koekemoer et al. 2011) and our own reduction (see McLure et al. 2011) of the Early Release Science (ERS) campaign (e.g., Windhorst et al. 2011). Colors were computed with respect to the  $z_{850}$  flux using matched apertures with up-to-date zero points, and total WFC3 magnitudes were derived by combining the measured colours with the total  $z_{850}$ -band flux.  $K_s$ -band photometry is taken from deep ISAAC imaging (Retzlaff et al. 2010) following the procedure discussed in Stark et al. (2009). For GOODS-N, we use near-infrared imaging obtained from CFHT/WIRCAM (Wang et al. 2010).

The rest-frame optical at  $z > 4$  is probed by the deep *Spitzer*/IRAC (Fazio et al. 2004) imaging of GOODS-S and GOODS-N (Dickinson et al. 2012, in prep). In particular, the  $3.6\ \mu\text{m}$  (hereafter [3.6]) and  $4.5\ \mu\text{m}$  (hereafter [4.5]) are the most useful, as the longer wavelength filters are typically not sensitive enough to detect most  $z > 4$  galaxies. As in Stark et al. (2009), we focus primarily on the subset of ACS-selected galaxies whose IRAC

fluxes are not contaminated significantly by neighboring sources. The IRAC magnitudes are measured in apertures  $2.4$  arcsec in diameter and to account for flux falling outside this aperture, we apply a  $0.7$  mag aperture correction derived from a sample of isolated point sources. Recognizing that selecting only isolated IRAC sources limits the size of our eventual sample, we included IRAC flux measurements for galaxies in GOODS-South from the MUSIC catalog (Grazian et al. 2006; Santini et al. 2009). These fluxes rely on a deconvolution procedure to extract fluxes from sources with contaminating neighbors. A comparison between the two photometry methods reveals consistency for our isolated sample, with a standard deviation of  $0.19$  mags and no systematic offset.

In total, we have 92 galaxies in the range  $3.8 < z < 5.0$  with measured IRAC photometry. In our analysis, we will focus on the subset of 45 galaxies with confident ( $>5\sigma$ )  $4.5\ \mu\text{m}$  detections (see Table 1), as without an accurate measure of the  $4.5\ \mu\text{m}$  flux it is impossible to infer the expected stellar continuum from population synthesis models. The objects with deconvolved GOODS MUSIC photometry make up 60% of the final sample.

Some caution must be exercised when applying inferences from a spectroscopic sample to the parent photometric population. In attempting to infer the typical level of rest-optical nebular contamination, we must be particularly careful that we do not bias our sample toward strong  $\text{Ly}\alpha$  emitting galaxies, a population which might have larger than average sSFR and  $H\alpha$  EW. For faint galaxies ( $z_{850} > 25.5$ ), the spectroscopic sample of Stark et al. (2010) is indeed biased toward  $\text{Ly}\alpha$  emitters. But by requiring a  $5\sigma$  detection in the [4.5] band, we limit our sample to brighter systems (average  $z_{850}$ -band magnitude of 25.0) for which we are more complete spectroscopically. Indeed the percentage of galaxies for which we measure  $\text{Ly}\alpha$  in emission is actually only 46%, highlighting the fact that many galaxies in this bright subset are instead confirmed via the combination of  $\text{Ly}\alpha$  in absorption and metal absorption lines (e.g., Jones et al. 2012). Furthermore, the fraction of galaxies in this subset with strong ( $\text{EW} > 50\ \text{\AA}$ )  $\text{Ly}\alpha$  emission (5%) is similar to that measured for galaxies in this  $M_{\text{UV}}$  and redshift range (6% in Stark et al. 2010) adding confidence that the sample we use in this paper is not likely to be strongly biased toward nebular emitters and appears fairly representative of the photometric population.

### 3. POPULATION SYNTHESIS MODELING

#### 3.1. Modeling Procedure

Our goal is to quantify the nebular contribution through analysis of the SEDs of a large spectroscopic sample at  $3.8 < z < 5.0$ . The advantage of our technique is that, for these sources, we can predict the exact wavelengths of rest-frame optical emission lines and thereby remove ambiguities associated with determining the photometric redshift simultaneously from contaminated broadband photometry.

Previous attempts to assess the impact of nebular emission on broadband photometry have utilized models which include the contributions from both nebular and stellar emission. For the reasons outlined in §1, our analysis will focus instead on models containing only stellar

continuum. The stellar continuum predictions are based on the models of Bruzual & Charlot (2003) and the technique we will adopt is mostly similar to that described in detail in Stark et al (2009). However, we also investigate how including nebular emission affects the derived physical properties. To do so, we make use of the code described in Robertson et al. (2010) to which the interested reader is referred. In this code, line emission is calculated from the number of ionizing photons per second, which is provided as output from our population synthesis models.

In the Robertson et al. (2010) code, the intensities of hydrogen lines are computed from the values tabulated in Osterbrock & Ferland (2006), assuming case B recombination. We compute the intensities of the lines of common metallic species from the empirical results of Anders et al. (2003), assuming a gas phase metallicity of  $Z = 0.2 Z_{\odot}$ , similar to that measured for galaxies at these redshifts (Maiolino et al. 2008, Jones et al. 2012). The recombination line luminosities are calculated assuming that the ionising photon escape fraction,  $f_{\text{esc}}$ , is 0.2 (see Shapley et al. 2011 for a discussion of expected escape fractions). Since we do not rely on the nebular models for our primary conclusions, this assumption does not affect our results. The continuum contribution from bound-free, free-free, and two photon continuum emission is also calculated following Osterbrock & Ferland (2006). The full nebular template is then added to each stellar continuum model, which is then used to calculate the synthetic fluxes used in our SED fitting code.

Since our sample has the virtue of precise spectroscopic redshifts, we do not fit the photometric bands spanning the Ly $\alpha$  forest and Ly $\alpha$  emission lines, both of which vary significantly from source to source at any given redshift. For the redshift range which we are primarily interested in ( $3.8 < z < 5.0$ ), this leaves 7-8 (largely) independent photometric constraints on the SED in GOODS-S and 6 constraints on GOODS-N. For consistency with the earlier literature, we consider a Salpeter (1955) initial mass function with 0.1-100  $M_{\odot}$ . Given the relatively small number of constraints on the SED, we utilize a moderately restricted grid, varying only the age, dust reddening, and normalization factor. We fix the star formation history as either constant or rising with time following the  $t^{1.7}$  power law inferred in Papovich et al. (2011). This restricted grid of SFH is supported by the results of Reddy et al. (2012) that demonstrate that at  $z \simeq 2$ , the star formation rates inferred from exponentially-declining star formation history models do not agree with those measured from the observed IR and UV fluxes. Nevertheless we have verified that our results would not be affected if we had adopted exponential decay models. Finally we utilize sub-solar metallicity ( $Z=0.2 Z_{\odot}$ ) motivated by the observations discussed above.

We allow the differential extinction,  $E(B-V)_{\text{stars}}$ , to range between 0.00 and 0.50 in steps of 0.02, and we limit the model ages to lie between 5 Myr and the age of the universe at the redshift of interest. The precise form of the dust attenuation curve is, of course, not known at  $z > 4$ , but we consider the reddening law appropriate for local starbursts (e.g., Meurer et al. 1999, Calzetti et al. 2000) and a steeper attenuation curve that is appropriate for the SMC (e.g., Gordon & Clayton 1998).

The latter appears to be appropriate for young galaxies ( $<100$  Myr) at high redshift (Siana et al. 2008, Reddy et al. 2010, 2012), a population which might become increasingly dominant at  $z > 4$ .

The relative extinction provided to stars and nebular emission is not definitively understood at high redshift. Expectations from nearby galaxies suggest that the nebular gas is preferentially more extinguished than the stellar continuum, as expected if the HII regions lie in dustier regions than the stars contributing to the integrated stellar continuum. Based on observations of local star-forming galaxies and starbursts, Calzetti et al. (2000) suggest that  $A_{V,\text{neb}} = A_{V,\text{SED}}/0.44$ . Whether or not this relationship holds at high redshift is unclear. Some of the first studies of H $\alpha$  emission in star forming galaxies  $z \simeq 2$  indicated that the nebular gas and stars might be equally attenuated (e.g., Erb et al. 2006, Reddy et al. 2010). But more recently, new studies have emerged which support a factor  $\simeq 2$  higher extinction toward HII regions (e.g., Forster-Schreiber et al. 2009, Onodera et al. 2010, Mancini et al. 2011, Wuyts et al. 2011), similar to that observed locally. Clearly an improved understanding of how the relative distribution of stars and HII regions depends on age and mass would greatly benefit attempts to simultaneously fit stellar and nebular emission via population synthesis models. In the nebular+stellar models presented in this paper, we will simply assume that  $A_{V,\text{SED}} = A_{V,\text{neb}}$ .

In the following, we will fit the data with both the nebular+stellar and stellar continuum models. For the latter, the cleanest method is obtained by fitting the data excluding the [3.6] flux measurement, given that this band could be contaminated by H $\alpha$ . However, excluding this band means that only one filter is available to constrain the SED beyond the Balmer Break. We therefore also fit the data using all photometric information, i.e. including the [3.6] measurement. This is discussed further in §3.2. For each galaxy, we compute the model age, normalization, and  $A_V$  which provide acceptable fits to the data. The normalization is then mapped to the star formation rate and stellar mass appropriate for the given template. We compute uncertainties on these parameters by bootstrap resampling the data within the allowed photometric uncertainties.

### 3.2. Nebular Line Strengths

We infer H $\alpha$  emission line strengths in our sample of  $3.8 < z < 5.0$  galaxies by comparing the observed flux density in the [3.6] bandpass to the flux density in that filter expected from stellar continuum alone. We explore the method which produces the most accurate equivalent widths below.

To verify the reliability of using the broadband flux excesses to derive emission line strengths, we examine the SEDs of a moderate redshift sample of nebular line emitters with spectroscopically-measured [OIII] line fluxes from WFC3 grism observations of the Hubble Ultra Deep Field (Trump et al. 2011). We choose this sample rather than larger ground-based samples because use of 2D grism spectroscopy avoids uncertainties owing to slit losses. To characterize the contribution of the emission lines to the broadband SEDs, we measure optical through mid-IR photometry using the UDF dataset (see McLure et al. 2011 for details) and perform population synthesis

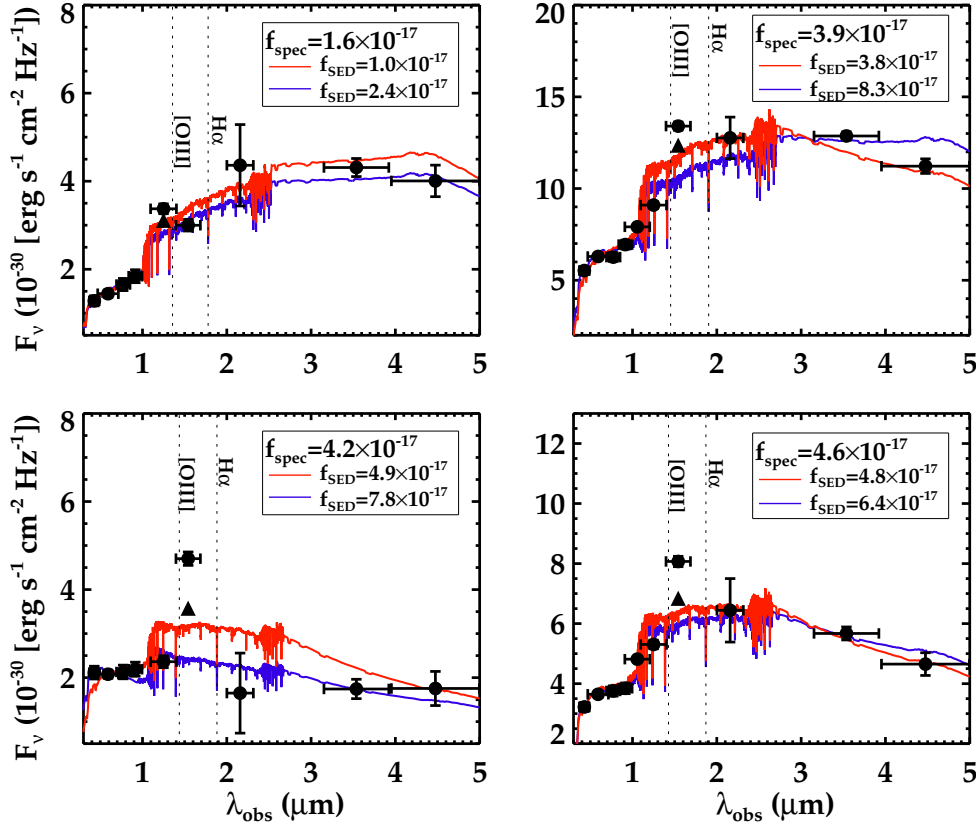


FIG. 2.— Verification of the flux excess method of measuring emission lines strengths. The four panels show SEDs of spectroscopically-confirmed galaxies with  $1.8 < z < 2.3$  for which measurements of emission line fluxes are available from the WFC3 grism study of Trump et al. (2011). The flux in the broadband filter contaminated by [OIII] is greater than that expected from the best-fitting stellar continuum models in each of the four SEDs. The two displayed stellar continuum models correspond to fits excluding the contaminated filter (blue bottom curve) and fits including all available optical and near-IR filters (red top curve). The flux density obtained by subtracting the directly-measured emission line contribution to the contaminated broadband flux is shown with a triangle. In each panel, we provide the [OIII] emission line flux measured with the WFC3 grism ( $f_{\text{spec}}$ ) and the the emission line flux inferred from the photometric excess of the contaminated filter with respect to the stellar continuum models ( $f_{\text{SED}}$ ) in units of  $\text{erg}/\text{cm}^2/\text{s}$ .

modelling following exactly the same procedure as described above. [OIII] will either fall in the J<sub>125</sub>-band (at  $1.3 < z < 1.8$ ) or H<sub>160</sub>-band (at  $1.8 < z < 2.3$ ). We characterize the likely strength of the emission lines by comparing the observed broadband flux (in the contaminated filter) to the stellar continuum flux expected from the best-fitting population synthesis models. We consider the stellar models with and without the contaminated bandpass included. In order to ensure a reliable measure of the stellar continuum in the vicinity of [OIII], we do not consider galaxies with strong emission lines in adjacent infrared filters (e.g., [OIII] in H<sub>160</sub> and H $\alpha$  in K<sub>s</sub>) or those undetected in K<sub>s</sub>-band.

We focus our analysis on the four systems in this remaining subset for which the measured [OIII] flux is predicted to make a significant (e.g.,  $\gtrsim 4\%$ ) contribution to the broadband photometry. In each of these systems, the contaminated filter reveals an excess with respect to the best-fitting stellar continuum model (Figure 2). The fluxes required to produce the broadband excesses in the contaminated filter agree well with those measured spectroscopically (Figure 2), with the results from the two fitting methods typically bracketing the observed line flux. While both methods produce remarkably good agreement, the line fluxes are slightly more accurate (av-

erage flux uncertainty of  $\simeq 20\%$ ) when the stellar continuum is estimated from the fit to the SED including the contaminated filter. When the contaminated filter is excluded from the fitting process, the inferred line flux is typically 1.5-2.0 $\times$  greater than measured with the WFC3 grism. Given the SEDs are fairly poorly sampled in the wavelength range where the continuum flux is required, it is conceivable that by excluding the contaminated filter, the fitting process will prefer redder models which fit the flux in the adjacent filters but underpredict the continuum in vicinity of the emission line of interest. Regardless of the precise reason, it is clear from Fig. 2 that by considering the results from both methods, fairly accurate line strengths can be extracted from the photometry.

The results of this test therefore motivate use of the broadband flux excesses to infer line strengths in carefully-selected spectroscopic samples at higher redshifts where direct spectroscopic measurements of nebular line fluxes are not yet available. As a result of the higher redshifts (and the corresponding  $1+z$  boost in observed equivalent width), we expect the nebular line contribution to broadband fluxes to be greater than typically observed at intermediate redshifts (e.g., Trump et al. 2011), allowing the flux excesses to more consistently stand out with respect to photometric uncer-



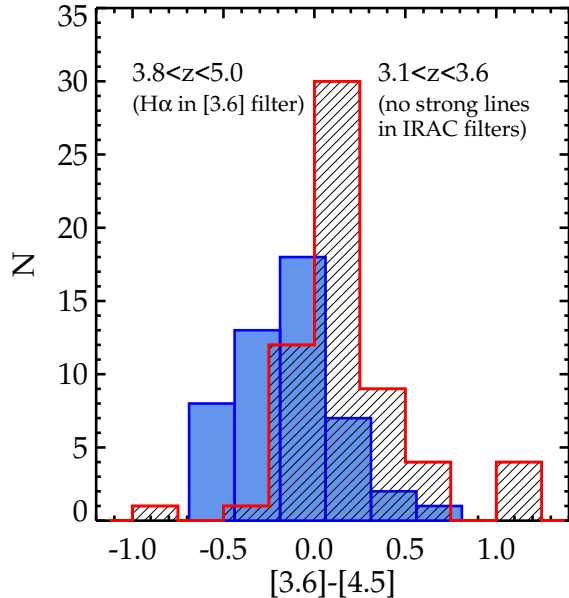


FIG. 3.— The effect of emission lines on broadband colors. The distribution of  $[3.6]-[4.5]$  colours for galaxies at  $3.8 < z < 5.0$  (blue filled histogram) and at  $3.1 < z < 3.6$  (red shaded histogram). The colours in the lower redshift sample reflect the reddened stellar continuum, as both filters are free from strong emission lines. In contrast, the colors of the  $3.8 < z < 5.0$  galaxies are shifted toward bluer values by  $H\alpha$  emission (which lies in the  $3.6\mu\text{m}$  bandpass).

tainties. Based on the results in this section, we expect the true line fluxes to be bracketed by our two fitting methods, with the most accurate measurements obtained by fits to the entire SED.

#### 4. RESULTS

We now discuss the results derived from applying our technique to the SEDs of spectroscopically-confirmed galaxies in the redshift range  $3.8 < z < 5.0$  over which  $H\alpha$  may contaminate the IRAC  $3.6\mu\text{m}$  filter. We compare the observed  $[3.6]$  flux densities to the stellar continuum expected from population synthesis models and use the results to infer an empirically-based  $H\alpha$  equivalent width distribution (§4.1). We discuss the possible redshift evolution of the nebular line strengths in §4.2. Using the empirically-derived equivalent width distributions, we examine how nebular emission affects the derived physical properties of  $z > 4$  galaxies (§4.3).

##### 4.1. Strength of Nebular Emission Lines

We begin by comparing the  $[3.6]-[4.5]$  colour distribution for galaxies at  $3.8 < z < 5.0$  with that for galaxies at  $3.1 < z < 3.6$  (a redshift range over which the IRAC colours are uncontaminated by strong nebular emission). This should reveal the impact of  $H\alpha$  emission on broadband fluxes at  $z > 3$ . We apply this test for 45 galaxies at  $3.8 < z < 5.0$  with robust flux measurements in the  $4.5\mu\text{m}$  filter which constrains the rest-optical stellar continuum. The results (Figure 3) point to a significant contribution from  $H\alpha$ . The median  $[3.6]-[4.5]$  colour at  $3.8 < z < 5.0$  is 0.33 mag bluer than the median value at  $3.1 < z < 3.6$ , consistent with expectations if  $H\alpha$  pollutes the  $3.6\mu\text{m}$  filter in the higher redshift bin. Note the

slightly red  $[3.6]-[4.5]$  colors of the  $3.1 < z < 3.6$  sample are exactly what is expected for moderately reddened ( $E[B - V] \simeq 0.1$ ) galaxies with a constant star formation history and luminosity-weighted ages of 100 Myr. A Kolmogorov-Smirnov test demonstrates with confidence that these two color distributions are distinct (KS statistic of  $D=0.54$  with an associated probability by chance of  $8 \times 10^{-8}$ ). We also consider whether the change in color might be due to photometric scatter from increased photometric error in the higher redshift bin. We test this by randomly perturbing the  $3.1 < z < 3.6$   $[3.6]-[4.5]$  colour distribution according to the IRAC flux errors of the  $3.8 < z < 5.0$  sample. While this can slightly broaden the width of the colour distribution, it does not shift the median colour to bluer values as observed.

While the most natural interpretation of the systematic offset is the presence of  $H\alpha$  in the  $[3.6]$  filter, it is conceivable that other effects could contribute. For example, one might expect that a systematic offset in  $[3.6]-[4.5]$  colours might arise from the slightly different rest-frame wavelengths sampled and the (potentially) younger ages in the higher redshift bin. Examination of population synthesis models indicates that intrinsic galaxy evolution is not likely to dominate the shift in  $[3.6]-[4.5]$  colors. Given the median reddening and ages inferred for the  $3.1 < z < 3.6$  and  $3.8 < z < 5.0$  spectroscopic samples, we would expect to see  $[3.6]-[4.5] \simeq 0.1$ . This is similar to that observed at  $3.1 < z < 3.6$ , but significantly redder than that observed in the  $3.8 < z < 5.0$  redshift range with  $H\alpha$  contamination. We therefore conclude that nebular contamination is likely the dominant cause of the differences in the  $[3.6]-[4.5]$  colours.

A particularly convincing verification of the above statistical test is the fact that we can directly see evidence of strong nebular emission in individual SEDs (Figure 4). Clearly in these examples the flux in the  $3.6\mu\text{m}$  filter is not only in excess of that at  $4.5\mu\text{m}$  but is also significantly in excess of the stellar continuum of the best-fitting population synthesis models. The SEDs of galaxies in this redshift range are (not surprisingly) typically better fit by models including nebular emission (blue lines in bottom panel cf. red lines in top panel for stellar continuum models in Figure 4).

To estimate the strength of  $H\alpha$ , we compute the amount by which the observed  $3.6\mu\text{m}$  flux exceeds the predicted stellar continuum flux. We define the  $3.6\mu\text{m}$  excess,  $\Delta[3.6]$  as the difference between the  $[3.6]$  magnitude expected from stellar continuum models which fit the SED and the observed  $[3.6]$  magnitude. Positive values indicate that the observed flux is greater than can be accommodated by stellar continuum. This test requires an accurate measure of the stellar continuum in the rest-optical. Again we limit our sample to those galaxies with confident  $[4.5]$  detections, as this filter (devoid of strong emission lines) is necessary to anchor the population synthesis models beyond the Balmer Break.

The distribution of  $3.6\mu\text{m}$  magnitude excesses in our spectroscopic sample (Figure 5) reveals that 96% of galaxies are observed to be brighter at  $[3.6]$  than predicted from the best-fitting stellar continuum models. The median excess, 0.27 mag, suggests that the typical rest-frame emission line equivalent width in the  $3.6\mu\text{m}$  filter at  $3.8 < z < 5.0$  is 360-450 Å. Emission lines therefore contribute nearly 30% of the observed  $[3.6]$  broad-

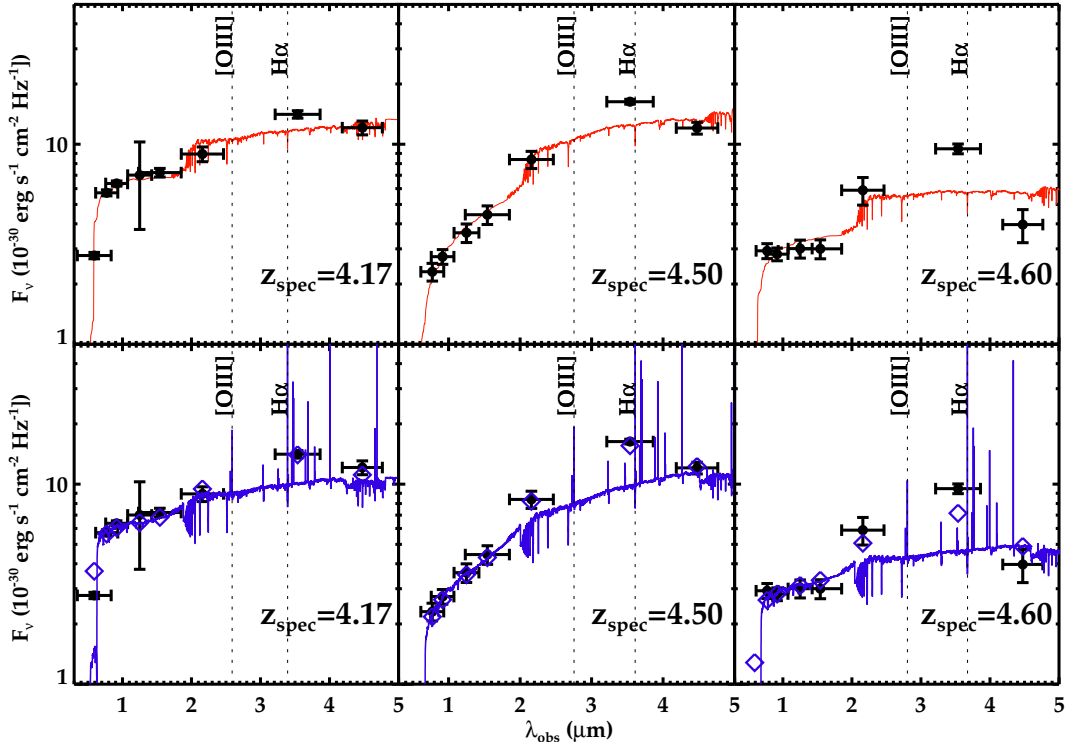


FIG. 4.— SEDs of spectroscopically confirmed galaxies at  $3.8 < z < 5.0$  fit using population synthesis models containing both stellar continuum (top row) and stellar+nebular emission (bottom row). Many galaxies in this redshift range show blue [3.6]-[4.5] colours, with the  $3.6\mu\text{m}$  flux significantly in excess of the best-fitting stellar continuum. This flux excess is strongly suggestive of  $\text{H}\alpha$  nebular line contamination. Not surprisingly, models containing nebular emission provide significantly better fits to the observed photometry, as clearly indicated by the agreement between the synthetic (open blue diamonds) and observed (solid black circles) in the bottom row. In the following, we will only consider objects for which the Balmer Break can be anchored by a significant ( $S/N > 5$ ) [4.5] detection, removing fainter objects (like that in the right panel) for which an accurate flux excess is difficult to extract.

band photometry. These values are derived from stellar continuum model fits that include the contaminated  $3.6\mu\text{m}$  filter in the modelling. As we demonstrated in §3, this method produces the most accurate flux estimates. If the contaminated filter is excluded from the modelling procedure, the inferred continuum level is typically reduced, resulting in a slightly larger median [3.6] excess (0.37 mag) and total equivalent widths (520-650 Å). Note these represent the equivalent width of all emission lines in the [3.6] filter. We derive the fractional contribution of  $\text{H}\alpha$  below. Based on the discussion in §3.2, it is likely that these measurements bracket the range of mean nebular emission line strengths in  $3.8 < z < 5.0$  galaxies. Reassuringly, this EW range is consistent with that required to explain the 0.33 mag offset in median [3.6]-[4.5] colors of  $3.1 < z < 3.6$  and  $3.8 < z < 5.0$  galaxies in Figure 3.

To estimate the *equivalent width distribution* of emission lines contaminating the IRAC  $3.6\mu\text{m}$  filter, we need to admit a range of equivalent widths to reproduce the observed  $3.6\mu\text{m}$  photometric excess distribution of Figure 5a. We assume that equivalent widths are distributed in a log-normal fashion, similar to that seen from  $\text{H}\alpha$  emission locally and at moderate redshifts (e.g., Lee et al. 2007, Ly et al. 2011). We consider a large grid spanning a range of  $\sigma$  and  $\mu$ , the width and mean of the equivalent width distribution. We translate each equivalent width into a  $3.6\mu\text{m}$  excess, applying a photometric scatter of 20% (a conservative estimate for the average  $3.6\mu\text{m}$

magnitude error) and compute the flux excess distribution expected from the input equivalent width distribution. We find that the observed flux excess distribution is well-fit by an equivalent width distribution with  $\sigma = 0.25$  and  $\langle \log_{10}(W_{[3.6]}/\text{Å}) \rangle = 2.57$  (Figure 5b). This equivalent width will surely be dominated by  $\text{H}\alpha$  emission, but other emission lines ([SII], [NII]) may of course contribute. The contribution of other lines will depend on the physical properties (e.g., metallicity) of the galaxies. Our sub-solar ( $0.2 Z_{\odot}$ ) metallicity models indicate that  $\text{H}\alpha$  should contribute  $\simeq 76\%$  of the observed equivalent width. In this case, the typical  $\text{H}\alpha$  EW at  $3.8 < z < 5.0$  is  $\langle \log_{10}(W_{\text{H}\alpha}/\text{Å}) \rangle = 2.45$ . With these assumptions, if the [3.6] filter is excluded from the fitting, we find  $\langle \log_{10}(W_{\text{H}\alpha}/\text{Å}) \rangle = 2.61$ . As above, we adopt this as an upper bound to the average  $\text{H}\alpha$  EW.

The level of  $\text{H}\alpha$  emission quoted above is actually very reasonable given the typical properties of  $z \simeq 4-5$  LBGs (e.g., Stark et al. 2009, Gonzalez et al. 2011a). For constant star formation, ionizing photon escape fraction of 0.2, and ages of  $\simeq 100-250$  Myr, we would expect  $\text{H}\alpha$  EWs to be  $\simeq 200-300$  Å, similar to the range we infer. So the observation of [3.6] excesses of 0.2-0.3 mag relative to stellar continuum (Figure 3) is exactly what we would expect given the shape of the overall SEDs. Indeed, the absence of any nebular contamination at  $3.8 < z < 5.0$  would have been a far more surprising finding.

#### 4.2. Evolution of Nebular EW Distribution

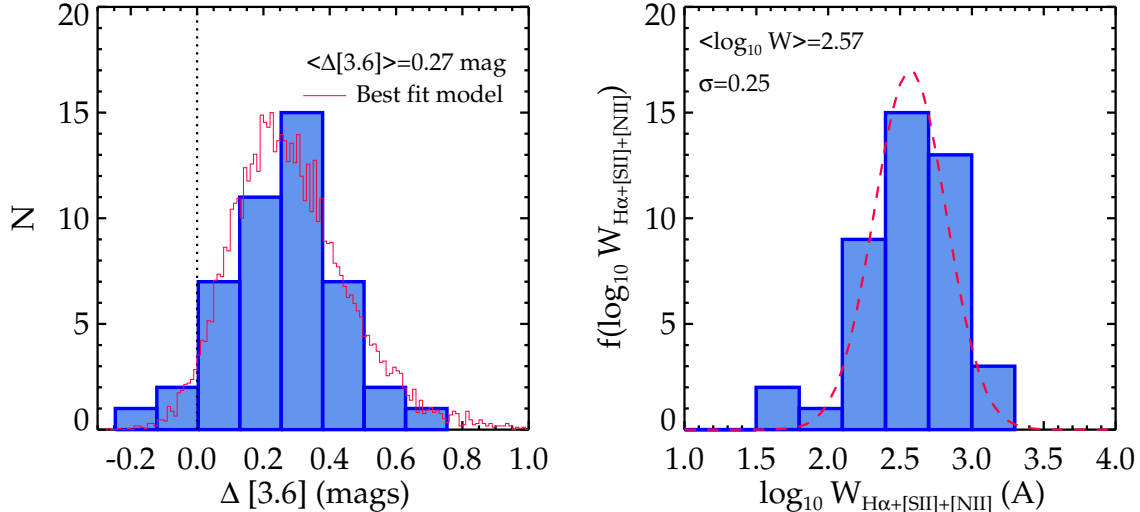


FIG. 5.— *Left:* The distribution of 3.6μm magnitude excesses ( $\Delta[3.6]$ ) in our  $3.8 < z < 5.0$  galaxy sample. The magnitude excess is defined as the difference between the [3.6] magnitude inferred from the stellar continuum of the best-fitting population synthesis model and the [3.6] magnitude observed with *Spitzer*/IRAC. The positive  $\Delta[3.6]$  values exhibited by our sample indicate that the stellar continuum is unable to account for the observed flux in the 3.6 μm filter. The magnitude excess distribution is well fit by a log-normal equivalent width distribution with  $\langle \log_{10} W \rangle = 2.57$  and  $\sigma = 0.25$  (red curve). *Right:* Distribution of equivalent widths required to reproduce the observed flux excesses (blue histogram) compared to the functional form we adopt for the equivalent width distribution (red curve).

Before evaluating how nebular emission affects the derived stellar masses at  $4 < z < 7$ , it is interesting to consider whether the nebular equivalent width distribution is likely to evolve with redshift. Fumagalli et al. (2012) recently examined the evolution of  $\text{H}\alpha$  equivalent widths at lower redshifts, finding that the evolution could be fit by a power law  $\propto (1+z)^{1.8}$  for galaxies with  $10^{10} M_{\odot}$  in stellar mass (Figure 6). While our sample size is too modest to permit a detailed comparison with this trend at  $z \gtrsim 4$ , it is of interest to consider how the EWs we derived in §4.1 compare to those at lower redshift. We note that the  $\text{H}\alpha$  equivalent widths presented in Fumagalli et al. (2012) include the contribution of [NII], while the nebular line strengths we infer from photometric excesses include the contribution of all emission lines contaminating the [3.6] filter. Using our  $0.2 Z_{\odot}$  population synthesis models, we estimate that 82% of the equivalent width inferred from [3.6] photometric excesses arises from  $\text{H}\alpha$  and [NII]. Note that this is slightly larger than the percentage estimated in the previous section owing to the addition of [NII] to the calculation.

Applying this factor to the mean equivalent widths presented in §4.1, we compare the  $\text{H}\alpha + [\text{NII}]$  equivalent widths at  $3.8 < z < 5.0$  to those at  $z \lesssim 2$  (Figure 6). It is clear that the line strengths derived at  $3.8 < z < 5.0$  are consistent with a continued increase in the  $\text{H}\alpha$  EW in the range  $2 \lesssim z \lesssim 5$ . While determination of the exact rate of increase is beyond the scope of this work, we note that the  $\text{H}\alpha$  EWs at  $3.8 < z < 5.0$  lie in the range expected by simple extrapolations of the power laws derived in Fumagalli et al. (2012). This increase in  $\text{H}\alpha$  EW over  $2 < z < 5$ , albeit tentative in nature, is supportive of an increase in the sSFR over  $z \gtrsim 2$ , consistent with more recent derivations (e.g., Bouwens et al. 2012).

Given these results, it is reasonable to expect nebular lines to be even stronger at  $z \simeq 6 - 7$ . Unfortunately, with both IRAC filters contaminated by strong emission

lines at these redshifts (Figure 1), we do not have a direct method of estimating the nebular line contamination in this regime. We thus will consider two cases in the following sections. First, we assume conservatively that the nebular line strengths remain fixed at the values derived at  $3.8 < z < 5.0$ . While a fixed EW might seem unlikely in light of the power law evolution at lower redshifts, we note that the rate of increase in the EW might slow if star formation histories transition into a phase of rapidly rising star formation rates (e.g., Finlator et al. 2011) at  $5 < z < 7$ . As a modest upper limit, we consider the case whereby the nebular equivalent widths continue to increase following a  $(1+z)^{1.8}$  power law. We conservatively adopt the mean EW of the fitting method including the contaminated [3.6] filter as the  $3.8 < z < 5.0$  reference value for this upper bound.

#### 4.3. Effect on $z \gtrsim 4$ Stellar Masses

In §4.1, we demonstrated that strong nebular line emission lines make a significant contribution to the broadband flux measurements at  $z > 3$ . If these lines are not accounted for in population synthesis modelling, the rest-optical stellar continuum (and thus the inferred stellar mass and age) will clearly be overestimated (e.g., Schaerer & de Barros 2010). In principle, these issues can be addressed through nebular+stellar population synthesis models described in §3. The drawback of this approach is that the ‘appropriate’ flux from nebular emission for any given model is very uncertain, depending not only on the escape fraction of ionizing radiation but also on the reddening law for the nebular gas, both of which are not known at  $z > 3$ .

Here we have attempted to account for these shortcomings using a method that relies on our empirically-derived nebular line equivalent width distribution. For each SED we wish to fit, we draw a large number ( $N \simeq 10^4$ ) of  $\text{H}\alpha$  emission line equivalent widths from the distribution we



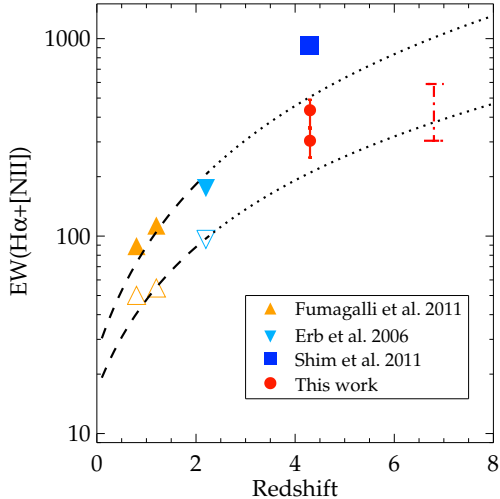


FIG. 6.— Evolution of the mean  $H\alpha+[NII]$  EW with redshift. The values at  $z < 4$  are as compiled in Fumagalli et al. (2012) for star forming galaxies with stellar mass in the range  $\log_{10}M_{\star}=10.0-10.5$ . The dashed lines show the power law that Fumagalli et al (2012) fit to the EW evolution at  $z \lesssim 2$  while the dotted lines show an extrapolation of this power law to  $z \gtrsim 2$ . The open symbols denote the EWs appropriate for entire galaxy population in Fumagalli et al. (2012), while the solid symbols denote estimates for the star-forming subset. The red circles show EWs inferred from the photometric excess method in this paper, with the lower value arising from SED fits including all filters, and the upper value derived from fits excluding the contaminated [3.6] filter (see §3.2 for details). The range of EWs illustrated at  $z \simeq 6-7$  represents nebular line strengths that we apply to SEDs in §4.3, with the lower limit assuming that nebular line strengths remain fixed with increasing redshift and the upper limit assuming they follow a  $(1+z)^{1.8}$  power law.

derived in §4.1 (e.g., Figure 5b). The contribution from [OIII] and  $H\beta$  (which contaminate the *Spitzer*/IRAC filters at  $z \gtrsim 5$ ) is obtained by scaling the  $H\alpha$  EW by 1.7-2.0 $\times$  (the exact value chosen at random from a uniform distribution), consistent with the flux ratios observed in sub-solar galaxies at  $z \simeq 2-3$  (e.g., Hainline et al. 2009, Bian et al. 2010, Erb et al. 2010, Richard et al. 2011) and those predicted by our nebular+stellar population synthesis models. If the galaxy’s redshift places any of these strong lines in the broadband filters we are fitting, we subtract the predicted nebular flux from the photometry.

In order to evaluate how the average properties of the various  $z \simeq 4-7$  dropout populations are affected by nebular emission, we consider *composite SEDs* for the B, V,  $i'$ , and  $z$ -band dropout populations (e.g., Stark et al. 2009, Labbé et al. 2010b, Gonzalez et al. 2011b) binned by rest-UV magnitude. For the purposes of this section, we limit our analysis to the most recent determinations of the composite SEDs (Labbé et al. 2010b, Gonzalez et al. 2011b), both of which take advantage of WFC3 photometry in the UDF and GOODS fields. Since the effect of nebular emission on derived physical properties is clearly redshift-dependent (c.f. Figure 1), we must account for the distribution of redshifts within a particular dropout sample. Thus for each realization of the nebular line EW distribution, we also select a redshift from the expected photometric redshift distribution of the dropout population under consideration (see e.g.,

Bouwens et al. 2012). We fit these realizations of the composite SEDs using the stellar continuum models described in §3. Physical properties are determined in a similar manner to that described in §3, with uncertainties derived from the  $1\sigma$  intervals of the large number of realizations of the equivalent width distribution.

The impact of nebular emission is clearly seen in the  $\log M_{\star} - M_{UV}$  scaling relations shown in Figure 7. These are determined for each dropout population with and without the nebular correction from the composite SEDs discussed above. The absolute magnitudes are unchanged in this analysis, so the changes shown are due only to the contamination of broadband light by nebular emission lines. As expected, the impact of nebular emission is strongest in the range  $5 < z < 7$  where nebular lines contaminate both IRAC filters. In contrast, the nebular correction is less severe for the B-drop ( $z \simeq 4$ ) population, since the *Spitzer*/IRAC  $4.5\mu m$  filter is devoid of strong emission lines throughout the redshift range covered by B-drops (Figure 1).

Assuming the nebular line EW distribution at  $z > 5$  remains identical to that determined at  $3.8 < z < 5.0$ , we find that the average stellar masses are reduced by factors of  $\times 1.1, 1.3, 1.6,$  and  $2.4$  for the dropout populations centered at  $z \simeq 4, 5, 6,$  and  $7$  respectively. If the nebular line strengths increase with redshift at  $z \gtrsim 5$  following a  $(1+z)^{1.8}$  power law (Figure 6; Fumagalli et al. 2012), the typical stellar masses are reduced by  $\times 1.9$  and  $4.4$  at  $z \simeq 6$  and  $7$  respectively. We emphasize that these represent average corrections applicable to the B, V,  $i'$ , and  $z$ -band dropout populations. Individual galaxies throughout this redshift range will of course be affected differently.

To summarize, we have used the equivalent width distributions derived in §4.1 to compute the likely contribution of nebular emission to broadband photometry. We find that stellar masses at  $z \gtrsim 6$  need to be revised downward by 2-4 $\times$ , with the precise correction depending on whether the EW of  $H\alpha$  and [OIII] emission continue to increase with redshift beyond  $z \simeq 5$ . This result has an important effect on the  $\log M_{\star} - M_{UV}$  scaling relation, which previously was thought to be largely constant with redshift at  $z > 4$  (e.g., Stark et al. 2009, Gonzalez et al. 2011, McLure et al. 2011). It is actually clearly evident in the uncorrected  $\log M_{\star} - M_{UV}$  relations presented in Figure 7 that without nebular corrections, the  $M_{\star}/L_{UV}$  ratios implied by the composite SEDs *increase* with redshift. Our analysis indicates that this finding is likely to be an artifact of nebular contamination. After correcting for line emission, we demonstrate that the  $M_{\star}/L_{UV}$  ratios are likely to decrease by  $\times 1.4-2.5$  with redshift over  $4 < z < 7$ . This result has important implications for derivation of the stellar mass density (§5.1) and specific star formation rate evolution (§5.2) discussed below.

#### 4.4. Effect of Nebular Continuum Emission

Nebular continuum emission can also contribute to the observed broadband flux density. Most importantly, the addition of nebular continuum reddens the intrinsic spectrum at young ages, thereby requiring less dust extinction to reproduce the observed colors. This can lead to a reduction in the derived star formation rates, in addition to the reduction in the stellar masses discussed earlier. The effects of nebular continuum can be seen in

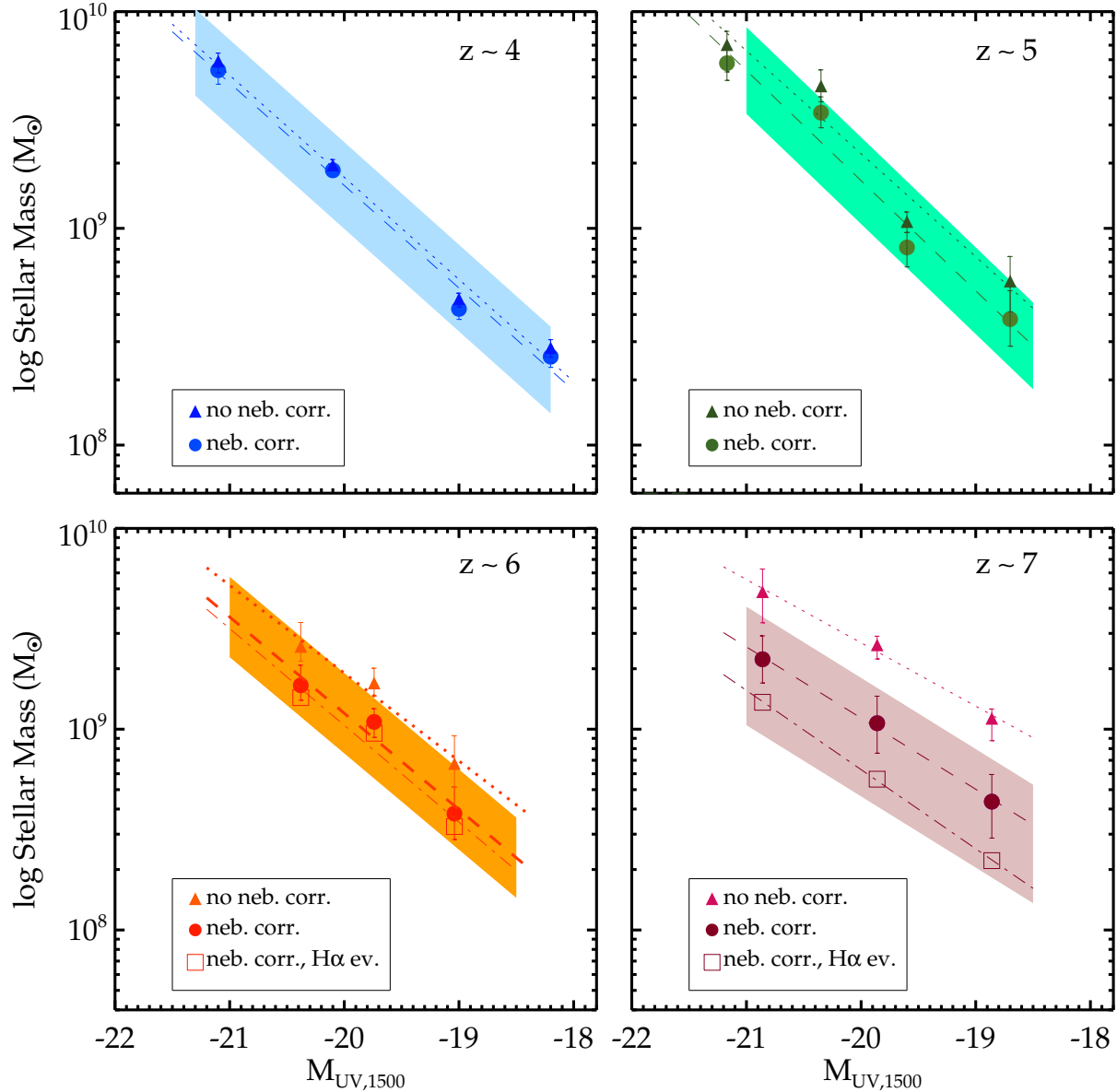


FIG. 7.— The impact of nebular emission on stellar mass derived using empirical determination of H $\alpha$  EW distribution at  $3.8 < z < 5.0$ . Solid circles show the  $\log M_{\star} - M_{UV,1500}$  relationship corrected for nebular contamination of broadband fluxes following the procedure discussed in §4.2. The dashed line gives the best linear fit to these data points. Solid triangles show the relationship with no correction for nebular emission assuming that the stellar continuum dominates the broadband flux. Without accounting for nebular emission, the  $\log M_{\star} - M_{UV,1500}$  relationship does not evolve much with redshift. However, incorporating nebular corrections, the normalization *decreases* by 1.4-2.5 $\times$  over  $4 < z < 7$ . The open squares correspond to nebular corrections derived assuming that the EW of nebular emission increases with redshift following the power law shown in Figure 6.

the nebular+stellar models, which typically display spectral edges in the vicinity of the Balmer/4000 Å break (bottom panel of Figure 4). Whether significant nebular continuum is actually contributing to the spectra of high- $z$  galaxies is unclear. Without better sampled SEDs (from e.g., medium-band near-IR photometry) that might probe such spectral edges, it is difficult to verify the presence of nebular continuum, as we are able to with nebular emission lines. Nevertheless if emission lines are very strong, it is likely that there is also a significant contribution from nebular continuum emission.

To quantify the likely impact of nebular continuum on the derived physical properties, we examine how the inferred dust reddening (and SFR) are affected when the nebular continuum is added. To do so, we compare the dust attenuation necessary to reproduce a fixed UV continuum slope for models with and without nebular continuum emission included. Assuming a Calzetti reddening law, we calculate the dust attenuation that reproduces a UV slope with  $\beta = -1.5$  as a function of model age. Owing to the redder intrinsic slopes, the inferred dust attenuation is reduced for the nebular+stellar models. The effect is most pronounced at the youngest ages,

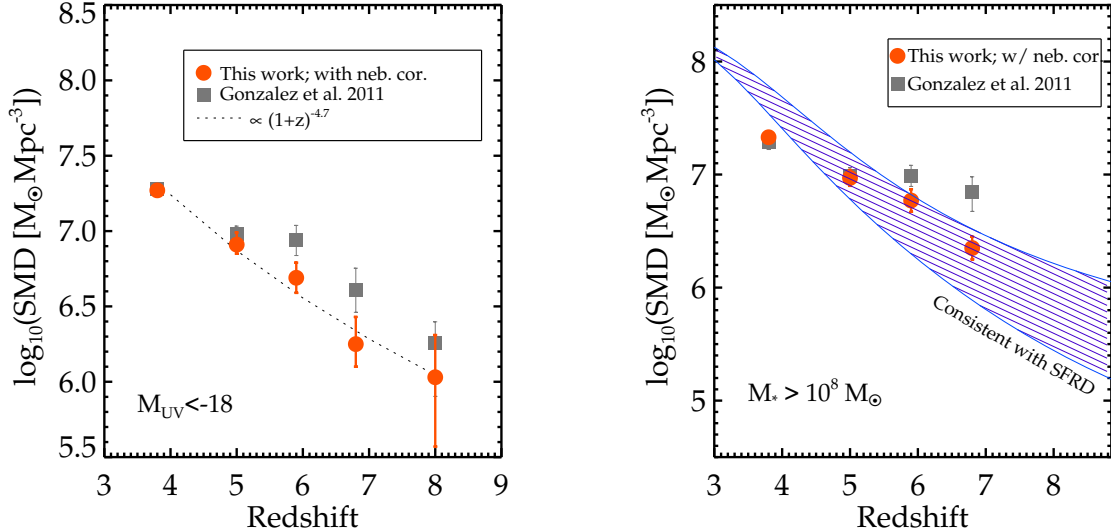


FIG. 8.— Evolution in the Stellar Mass Density: The mass density is computed by integrating the stellar mass function to a fixed UV luminosity limit (left panel) and fixed stellar mass limit (right panel). The main advance with respect to earlier work is the inclusion of corrections for nebular emission contamination of *Spitzer*/IRAC filters. These are computed using the nebular EW distribution derived from our spectroscopic sample in §4.1 and assume the H $\alpha$  EW distribution continues to evolve as a power law at  $z \gtrsim 5$ . The stellar mass functions are derived by combining the nebular-corrected  $\log M_{\star}$ - $L_{UV}$  relation with the UV luminosity functions presented in Bouwens et al. 2012. We assume that the scatter in the  $\log M_{\star}$ - $L_{UV}$  relation is  $\sigma \simeq 0.5$ , consistent with previous studies (e.g., Gonzalez et al. 2011a). The blue swath in the right panel shows the stellar mass density implied by the evolving star formation rate density, computed by integrating the UV luminosity functions (see Robertson et al. 2010 for details).

with the inferred attenuation up to 20% lower for nebular+stellar models with ages  $<30$  Myr. As a result of the reduced attenuation, a lower normalization is required to match the observed flux density, bringing down the inferred star formation rates by up to the  $\simeq 20\%$  level for the youngest systems. In practice, the impact of nebular continuum is more complicated and non-trivial to predict, depending strongly on the shape (i.e. age) of the observed SED. Given these uncertainties, our analysis in the following sections will focus on how physical properties are affected by nebular emission lines.

## 5. DISCUSSION

In the previous section, we used the broadband SEDs of a large sample of spectroscopically-confirmed galaxies to infer the distribution of nebular line strengths in UV-selected galaxies at  $3.8 < z < 5.0$ . We showed that the stellar masses inferred from population synthesis modelling are reduced at  $z > 5$  when the contribution of these lines to broadband flux densities is removed. In this section, we consider the implications of these results for our current picture of early mass assembly.

### 5.1. Stellar Mass Density at $z > 3$

In §4.2, we quantified the extent to which the stellar masses of  $z > 3$  galaxies are affected by nebular emission. Here, we seek to utilize these results to estimate the stellar mass density (SMD) evolution at  $z > 3$ . To derive the mass densities, we combine the  $\log M_{\star}$  -  $M_{UV}$  relationship with UV luminosity functions (LFs) in a manner mostly similar to that outlined in Gonzalez et al. (2011). Briefly, we extract a large number ( $N \simeq 10^5$ ) of luminosities from the measured UV LFs (e.g., Bouwens et al. 2011). We convert these luminosities to stellar masses using the  $\log M_{\star}$  -  $M_{UV}$  relationship, and an estimate of

the scatter about the median. Whereas earlier studies held the  $\log M_{\star}$  -  $M_{UV}$  relationship fixed with redshift at  $z \gtrsim 4$ , the strong redshift dependence of nebular contamination (Figure 1) forces us to reconsider the evolution of  $M_{\star}/L_{UV}$  ratios with redshift.

We compute the slope and normalization of the  $z \simeq 4$   $\log M_{\star}$  -  $M_{UV}$  relationship using the large sample of LBGs discussed in Stark et al. (2009). For simplicity, we assume the slope remains constant at  $z \gtrsim 4$  and consider only evolution in the normalization of the relationship. To compute the zero-points of the  $\log M_{\star}$  -  $M_{UV}$  relation at  $z \simeq 5, 6$ , and 7, we adjust the measured  $z \simeq 4$  relation to account for the relative normalisation of the nebular-corrected  $\log M_{\star}$  -  $M_{UV}$  relationships shown in Figure 7. To obtain a tentative estimate of the  $z \simeq 8$  stellar mass density, we apply the  $z \simeq 7$   $\log M_{\star}$  -  $M_{UV}$  relationship to the  $z \simeq 8$  UV LF. In all cases, we use the nebular corrections derived assuming an evolving H $\alpha$  EW distribution (see Figure 7), but we also discuss how these results would change if the EW distribution remains fixed at  $z > 5$ .

In addition to measurement of the  $\log M_{\star}$  -  $M_{UV}$  relationship, accurate determinations of the dispersion are necessary to account for low luminosity galaxies with large  $M_{\star}/L_{UV}$  ratios. If scatter is not accounted for, the mass functions will be incomplete and mass densities (above a fixed mass limit) will be underestimated. While a measurement of the observed scatter at  $z \simeq 4$  (0.5 dex) was made in Gonzalez et al. (2011a), the intrinsic scatter is likely lower due to systematic uncertainties in the modelling as well as the effects of nebular contamination. In the following, we assume the intrinsic scatter is in the range 0.2-0.5 dex.

We focus first on the UV luminosity limited measure of

the SMD, considering only those galaxies with luminosities greater than  $M_{UV} = -18$ . The results are presented in Figure 8. As discussed in earlier sections, if nebular emission is not accounted for in the modelling, the inferred  $M_*/L_{UV}$  ratios actually increase moderately with redshift, leading to artificially high stellar mass densities at  $z \gtrsim 5$ . The inclusion of nebular emission reduces the mass density at  $z \simeq 7$  by up to  $4\times$ , while having little effect at  $z \simeq 4$ . As a result of these redshift-dependent corrections, the evolution in the SMD is fit by a steeper power law ( $[1+z]^{-4.7}$ ) than reported previously.

We also consider the SMD in galaxies with stellar masses in excess of  $10^8 M_\odot$ . For consistency with earlier measurements of the SMD, the measurements we present in Figure 8 assume that the  $\log M_* - M_{UV}$  relationship has an intrinsic dispersion of 0.5 dex. If the scatter is instead only 0.2 dex, for example, we would find stellar mass densities that are  $\simeq 1.6 - 2.0\times$  lower.

While previous estimates of the  $6 \lesssim z \lesssim 7$  SMD appeared broadly consistent with the integral of the  $z \gtrsim 7$  SFRD (after an appropriate correction for stellar mass loss and recycling), the SMD appeared to be on the high end of the range implied by the SFRD (e.g., Robertson et al. 2010). We compare our revised SMD to those implied by the SFRD in the right panel of Figure 8. The mass density implied by the SFRD is calculated in a similar manner as Robertson et al. (2010), updated to include the latest measurements of the UVLF (Bouwens et al. 2011). With appropriate corrections for nebular emission, the mass densities now appear in better agreement with the integrated SFRD.

The stellar mass density provides a useful integral constraint on earlier star formation. *Spitzer* observations of galaxies at  $z \simeq 6 - 7$  therefore offer a valuable measure of the likely ionizing output of galaxies at  $7 \lesssim z \lesssim 15$ . Therefore as measurements of the stellar mass density become more reliable, they will offer insight into the contribution of galaxies to reionization, complementing inferences from the UV luminosity function.

We have demonstrated in this paper that corrections for nebular emission are a crucial aspect of obtaining a reliable census of stellar mass in the early universe. In light of the reduced mass density required by nebular contamination, we re-consider the ability of galaxies to achieve reionization by  $z \gtrsim 6$ , updating the calculation presented in Robertson et al. (2010). Given the consistency with the SFRD (Figure 8), these results are not surprisingly similar to inferences obtained from the UV LF (e.g., Bouwens et al. 2012a; Kuhlen & Faucher-Giguère 2012). The UV output implied by the mass density is in principle sufficient to achieve reionization by  $z \simeq 6 - 8$  but struggles to account for the optical depth to electron scattering implied by WMAP (e.g., Larson et al. 2011).

Understanding this photon shortfall will require improved knowledge of how much star formation occurs beyond  $z \simeq 10$ . While direct detection of  $z \gtrsim 10$  galaxies will likely have to wait until JWST, *Spitzer* offers a unique means of progress in the coming years. By obtaining stellar mass estimates for the emerging samples of  $z \simeq 9 - 10$  galaxies (e.g. Bouwens et al. 2011b, Zheng et al. 2012), it will be possible to obtain some of the first constraints on the contribution of galaxies to the cosmic ionisation history beyond  $z \simeq 10$ .

## 5.2. *sSFR Evolution*

The reduced stellar masses we infer in §4 clearly will affect the evolution of the *sSFR* at  $z > 4$ . To estimate the impact, we compute the *sSFR* in fixed stellar mass bins using a similar approach as for the stellar mass function. We draw a large number ( $N \simeq 10^5$ ) of luminosities from the latest measures of the  $z \simeq 4 - 7$  UV LFs (Bouwens et al. 2012a). For each luminosity and redshift bin, we compute a stellar mass using the  $\log M_* - M_{UV}$  relationship derived in §4.1. We consider the case in which the strength of nebular emission is constant at  $z \gtrsim 4$  and also that in which the emission line equivalent widths increase with redshift (e.g., Figure 6).

The SFR is computed from  $M_{UV}$  through a series of steps. We account for dust extinction using the UV continuum slopes. For each realisation of the UV LF, we draw a UV slope,  $\beta$ , by adopting the redshift-dependent  $\beta - M_{UV}$  scaling relationships (Bouwens et al. 2012b). The UV slope is then converted to a dust attenuation factor at 1600 Å via the Meurer et al. (1999) IRX- $\beta$  relation ( $A_{1600} = 4.43 + 1.99\beta$ ). The UV luminosity is converted to SFR following the canonical Madau et al. (1998) and Kennicutt et al. (1998) relation  $L_{UV} = (\text{SFR}/M_\odot \text{ yr}^{-1}) 8.0 \times 10^{27} \text{ ergs s}^{-1} \text{ Hz}^{-1}$ . This relationship assumes a 0.1-125  $M_\odot$  Salpeter IMF and constant star formation rate of  $\gtrsim 100$  Myr. Finally, by examining the SFR and  $M_*$  of these realizations, we compute the median *sSFR* of the four dropout samples with stellar mass of  $5 \times 10^9 M_\odot$ . Before examining the results of this calculation, we discuss two important issues that we have hitherto neglected.

First we consider how the *sSFR* is affected by scatter in the  $\log M_* - M_{UV}$  relationship. Note that the *sSFR* will be *overestimated* if one merely uses the  $\log M_* - M_{UV}$  relation without taking into account the abundant population of lower SFR objects with large  $M_*/L_{UV}$  ratios. This issue is dealt with in detail in Reddy et al. (2012) for galaxies at  $z \simeq 2 - 3$ . Unfortunately, as we discussed in §5.1, the intrinsic scatter is very poorly constrained in UV-selected samples at  $z \gtrsim 4$ . As a result, previous estimates of the *sSFR* at  $z > 4$  have not accounted for  $M_*/L_{UV}$  scatter. To estimate how this shortcoming would affect the *sSFR*, we add  $\log M_* - M_{UV}$  scatter to the LF realization method described above. If the 0.5 dex observed  $z \simeq 4$  scatter reported in Gonzalez et al. (2011a) is entirely intrinsic, then the median *sSFR* would be reduced by  $2.8\times$  at  $z \simeq 4$ . Note that one might find slightly different adjustments for the same scatter at other redshifts owing to evolution in the luminosity function. In §5.1, we suggested that the intrinsic scatter is likely lower as systematic uncertainties in modelling (including uncertainties in the nebular corrections) surely broaden the dispersion in the stellar masses at fixed UV luminosity. In this case, fewer low SFR galaxies contribute to the *sSFR* distribution at fixed mass, resulting in a larger median *sSFR*. For example, a scatter of 0.2 dex would translate into a reduction of just  $1.2\times$  with respect to the case of no scatter. Physically, one may expect that the scatter at fixed luminosity would increase somewhat between  $z \simeq 7$  and  $z \simeq 4$ , as galaxies have had more time to undergo punctuated episodes of star formation which elevate both their star formation rates and mass off of the main sequence. We consider these possibilities in our discussion below.

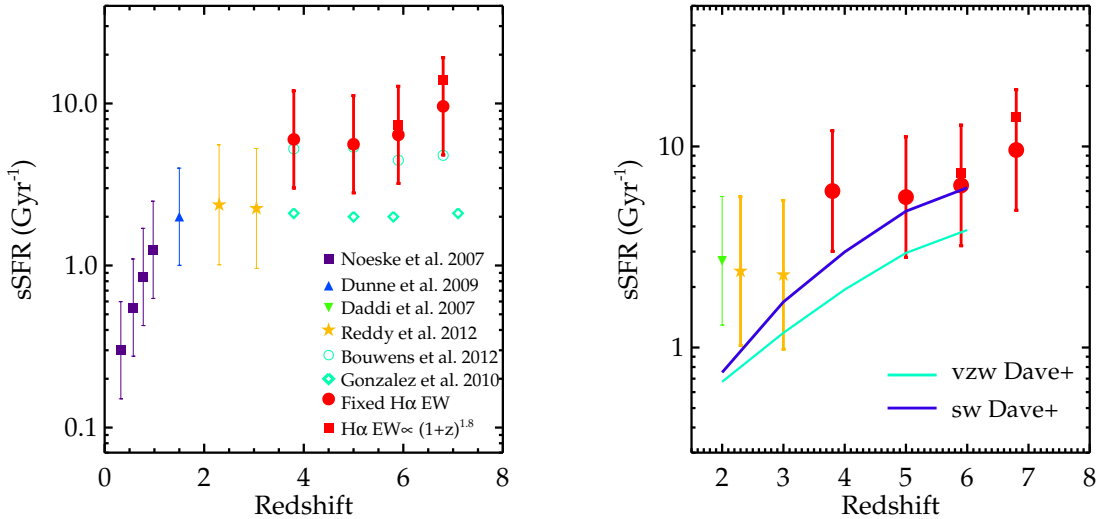


FIG. 9.— *Left:* Evolution in the specific star formation rate (sSFR). Our new measurements include stellar masses corrected for nebular emission line contamination. The solid red circles at  $z > 4$  show values derived assuming the nebular line EW distribution at  $4 < z < 7$  remains identical to that derived at  $3.8 < z < 5.0$  (Figure 5). The solid squares correspond to values obtained when an evolving nebular line EW distribution is adopted. The error bars show the assumed scatter about the mean sSFR taken from Reddy et al. (2012). *Right:* Comparison of observed sSFR to contemporary theoretical models. The solid lines show the sSFR evolution predicted from cosmological simulations discussed in Davé et al. (2011), with the blue line corresponding to their “slow wind” model and the light green line corresponding to the momentum driven wind “vzw” model. These models provide adequate fits at the highest redshifts ( $z > 5$ ) but undershoot the observed values at  $z \simeq 2 - 4$ .

We now examine a second issue which pushes the sSFR in the opposite direction. In particular, we examine how scatter (and perhaps systematic offsets) in the conversion between dust-corrected  $L_{UV}$  and SFR affect our sSFR determination. The conversion between UV luminosity and SFR that we use is valid for galaxies with model ages in excess of 100 Myr. Above this age, the conversion factor changes little for an assumed constant star formation history. But below 100 Myr, a larger SFR is required to produce a fixed  $L_{UV}$  (see Figure 25 of Reddy et al. 2012). For example, a galaxy with model age of 10 Myr requires a  $1.8\times$  larger SFR to reproduce the same  $L_{UV}$  as a galaxy with 100 Myr. With the reduced ages implied by the nebular corrections, it seems likely that such young systems are present in  $z \gtrsim 4$  dropout samples. Inclusion of dispersion in the model ages will preferentially shift the median SFR to larger values, resulting in somewhat larger sSFR. Furthermore, it is of course conceivable, if not likely, that such young systems will become more common both at higher redshift, requiring a systematic shift toward higher sSFR at earlier times.

We now turn to the derived sSFR evolution, which is shown in Figure 9a. First, ignoring the effect of nebular emission and the scatter discussed above, we find that the sSFR actually *decreases* marginally with redshift over  $4 < z < 7$ , similar to the findings of Bouwens et al. (2012b). This is driven largely by the redshift-dependence of the UV continuum slope  $\beta$  versus  $M_{UV}$  relationship. Galaxies at higher redshifts have bluer UV continua (e.g., Bouwens et al. 2012b, Finkelstein et al. 2012), reducing the dust-corrected SFR for a given  $M_{UV}$ . Considering the fixed  $M_*/L_{UV}$  ratios assumed in previous studies (e.g., Stark et al. 2009, Gonzalez et al. 2010), it is straightforward to understand this result. As we have discussed above, without nebular corrections, the data actually support a mild increase in the  $M_*/L_{UV}$

ratios with increasing redshift at  $z \gtrsim 4$  (Figure 7); if the  $M_*/L_{UV}$  ratios weren’t held fixed (and nebular emission not considered), one would have derived a more rapid decrease in sSFR at  $z > 4$ .

Incorporating our corrections for nebular emission reduces the  $M_*/L_{UV}$  ratios in the  $z \simeq 5 - 7$  LBG samples, increasing the sSFR in this redshift range. If the nebular line EW distribution at  $z \gtrsim 5$  is similar to that seen in Figure 5b, we find that the sSFR of galaxies with fixed stellar mass begins to show evidence for positive evolution with redshift, with the  $z \simeq 7$  value ( $9.6 \text{ Gyr}^{-1}$ )  $4\times$  larger than that at  $z \simeq 2$ . This can be viewed as a conservative estimate of the sSFR evolution. As we have argued, however, it is more likely that the equivalent width of H $\alpha$  and [OIII] *increase* in strength with redshift at  $z \gtrsim 4$ , consistent with the evolution seen at intermediate redshift (Fumagalli et al. 2012). Under these assumptions, the derived sSFR shows greater redshift evolution, with the  $z \simeq 7$  sSFR ( $14 \text{ Gyr}^{-1}$ ) roughly  $6\times$  greater than that at  $z \simeq 2$  (Reddy et al. 2012). While intrinsic scatter in the  $M_*/L_{UV}$  ratios might bring these numbers down somewhat (perhaps explaining the excess seen at  $z \simeq 4$ ), this is likely counteracted somewhat by scatter and/or systematic evolution in the SFR/ $L_{UV}$  ratios and possibly a shift toward reduced scatter in the  $M_*/L_{UV}$  ratios at higher redshifts.

To summarize, with the new dust corrections (Bouwens et al. 2012b) and adjustments for nebular emission contamination, we now find evidence for a power law increase in the sSFR at  $z \gtrsim 2$  that is much more consistent with theoretical expectations than previous observations indicated. Both the absolute values and rate of increase of the sSFR we derive at  $z \gtrsim 5$  are very similar to those predicted in the simulations of Davé et al. (2011a). Intriguingly the sSFR at  $2 < z < 4$  still remains moder-



ately in excess of theoretical expectations. As we have discussed above, the  $z \simeq 4$  estimate of the sSFR might come down somewhat owing to scatter in the  $M_*/L_{UV}$ . But the  $z \simeq 2-3$  sSFR measurements include the effects of scatter, so the discrepancy remains puzzling, especially in light of the emerging agreement at  $z \gtrsim 5$ . Previous theoretical studies have focused on a variety of explanations for the tension at  $z \simeq 2$ , including a time-varying initial mass function (e.g., Davé 2008, Narayanan & Davé 2012). Continued efforts along these lines are required to simultaneously explain the high sSFR at  $z \simeq 2$  along with the revised  $z \gtrsim 4$  sSFR estimates (Fig. 9).

Recall that previous indications of a nearly flat sSFR in fixed stellar mass bins at  $z > 2$  required a mechanism by which star formation is made increasingly inefficient at earlier times. Possibilities included the inefficient formation of molecular hydrogen in metal-poor galaxies (e.g., Robertson & Kravtsov 2008; Gnedin et al. 2009; Krumholz & Dekel 2012), or an increase in the mass outflow rate per unit star formation with redshift. The updated estimates of the  $z > 3$  sSFR no longer obviously require a significant suppression of star formation in galaxies with stellar mass in excess of  $10^9 M_\odot$ . The current measurements seem consistent with a picture whereby the rapidly increasing baryon accretion rates translate into higher sSFR at earlier times.

As with the stellar mass density, there is room for considerable improvements to these estimates in the coming years. By providing more individual detections of UV-faint galaxies, deeper *Spitzer* data will enable improved measurements of the slope and scatter of the  $\log M_* - M_{UV}$  relationship in the redshift range considered in Figure 9. It is also of interest to extend these measurements to  $z \simeq 8$ . In this redshift regime, [OIII] lies in the  $4.5\mu\text{m}$  filter, while the  $3.6\mu\text{m}$  filter is devoid of strong lines. Thus, with deep *Spitzer* data, the SEDs of  $z \simeq 8$  systems enable a unique method of deciphering how the strength of nebular emission evolves over  $5 \lesssim z \lesssim 8$ , one of the key uncertainties in the current analysis.

## 6. SUMMARY AND CONCLUSIONS

Measurement of the evolving stellar mass and sSFR distributions have proven critical to our understanding of early galaxy assembly and the UV photon budget of reionization-era galaxies. Recently, it has become clear that many of these early estimates might be significantly in error due to the contamination of the *Spitzer*/IRAC bandpasses by nebular emission lines. Knowledge of the strength of these emission lines is necessary for robust determinations of the stellar mass density and sSFR evolution. As these emission lines are shifted out of the observed atmospheric window, direct spectroscopic measurements will not be feasible until JWST.

In this paper, we present a method which enables constraints on nebular emission at  $z > 4$  by combining large spectroscopic samples and deep *Spitzer* photometry. Like Shim et al. (2011), we focus on the redshift range  $3.8 < z < 5.0$ , over which the IRAC [3.6] filter is contaminated by strong emission lines ( $H\alpha$ , [NII], [SII]) while the [4.5] filter is free of nebular contamination. Examining a carefully-selected subset of 45 galaxies, we find that the  $3.6\mu\text{m}$  flux is systematically in excess of the expected stellar continuum flux, revealing the presence of strong

nebular emission. No excess is seen in a spectroscopic sample at  $3.1 < z < 3.6$ , a redshift range over which no strong emission lines contaminate the IRAC filters. We use the photometric excesses in the contaminated [3.6] filter to estimate the equivalent width distribution of  $H\alpha$  emission at  $3.8 < z < 5.0$ . Equipped with this measure of nebular emission at high-redshift, we re-evaluate the evolution in the sSFR and stellar mass density at  $z \gtrsim 4$ . Our primary conclusions from this analysis are summarized below.

1. We find that the mean equivalent width of emission lines contaminating the [3.6] filter is  $\langle \log_{10}(W_{3.6}/\text{\AA}) \rangle \simeq 2.57 - 2.73$ . We estimate that  $\simeq 76\%$  of this signal arises from  $H\alpha$ , implying an average  $H\alpha$  equivalent width of  $\langle \log_{10}(W_{H\alpha}/\text{\AA}) \rangle \simeq 2.45 - 2.61$  at  $3.8 < z < 5.0$ .

2. The mean  $H\alpha$  equivalent width inferred at  $3.8 < z < 5.0$  appears greater than that for similar star-forming samples at lower redshifts. While definitive knowledge of the evolution in the  $H\alpha$  EW surely awaits direct spectroscopic measurement, the evolution we infer over  $2 \lesssim z \lesssim 5$  is certainly consistent with the  $(1+z)^{1.8}$  power law derived in Fumagalli et al. (2012). This likely reflects an increase in the sSFR at  $z \gtrsim 2$ , and importantly suggests that the EW of nebular emission continues to increase at  $z \gtrsim 5$ .

3. Using the  $H\alpha$  EW distribution we derive at  $3.8 < z < 5.0$ , we explore how nebular contamination is likely to affect the physical properties of galaxies at  $z > 3$ . We find that the stellar masses are reduced, on average, by 1.1, 1.3, 1.6, and  $2.4\times$  for dropout samples with mean redshifts of  $z \simeq 4, 5, 6,$  and  $7$ , respectively. If the equivalent widths of nebular lines continue to increase in amplitude at  $z \gtrsim 5$ , we estimate that the reduction in the stellar masses are likely to increase to  $1.9$  and  $4.4\times$  at  $z \simeq 6$  and  $7$ . We note that these corrections are representative for average measures of the dropout populations and not individual galaxies.

4. As the stellar mass density provides a valuable integrated measure of early star formation, constraints on the level of nebular contamination are critical to our knowledge of the ionizing photon budget of galaxies throughout the reionization era. After correcting for nebular emission contamination, we find a factor of  $\simeq 2\times$  reduction from previous estimates. The downward revisions to the stellar mass density improve consistency with expectations from the integrated star formation rate density. Extending such nebular-corrected measurements to emerging galaxy samples at  $z \simeq 8-9$  will yield an integral constraint on the UV photon budget during  $z \simeq 10-15$ .

5. Whereas previous derivations showed little evolution in the sSFR of fixed mass galaxies over  $2 < z < 7$ , we demonstrate that after accounting for nebular emission and correcting for dust, the sSFR increases by  $4-6\times$  over  $2 < z < 7$ . The absolute sSFR values inferred at  $z \gtrsim 5$  appear largely similar with predictions from simulations. While there certainly remains room for improvement (in both the data and the modelling), the increase in the sSFR at  $z \gtrsim 4$  seems consistent with a picture whereby increasing baryon accretion rates at larger redshift translate into larger sSFR in galaxies of a fixed stellar mass.

## ACKNOWLEDGMENTS

We are grateful to Rychard Bouwens, Romeel Davé, Desika Narayanan, Ivo Labbé, Masami Ouchi, Naveen Reddy, Daniel Schaerer, and Valentino Gonzalez for useful conversations. We thank Romeel Davé for making the results of his simulations available to us. DPS acknowledges support from NASA through Hubble Fellowship grant #HST-HF-51299.01 awarded by the Space Telescope Science Institute, which is operated by the Association of Universities for Research in Astronomy, Inc, for NASA under contract NAS5-26555. BER is partially supported through STScI grant HST-GO-12498.12-A. Support for Program number HST-GO-12498.12-A was provided by NASA through a grant from the Space Telescope Science Institute, which is operated by the As-

sociation of Universities for Research in Astronomy, Incorporated, under NASA contract NAS5-26555. JSD acknowledges the support of the European Research Council via the award of an Advanced Grant. JSD and RJM acknowledge the support of the Royal Society via a Wolfson Research Merit Award and a University Research Fellowship respectively. Some of the data presented herein were obtained at the W.M. Keck Observatory, which is operated as a scientific partnership among the California Institute of Technology, the University of California and the National Aeronautics and Space Administration. The Observatory was made possible by the generous financial support of the W.M. Keck Foundation.

## REFERENCES

- Anders, P., & Fritze-v. Alvensleben, U. 2003, *A&A*, 401, 1063
- Bian, F., Fan, X., Bechtold, J., et al. 2010, *ApJ*, 725, 1877
- Bouché, N., Dekel, A., Genzel, R., et al. 2010, *ApJ*, 718, 1001
- Bouwens, R. J., Illingworth, G. D., Franx, M., & Ford, H. 2007, *ApJ*, 670, 928
- Bouwens, R. J., Illingworth, G. D., Oesch, P. A., et al. 2011, *ApJ*, 737, 90
- Bouwens, R. J., Illingworth, G. D., Labbe, I., et al. 2011, *Nature*, 469, 504
- Bouwens, R. J., Illingworth, G. D., Oesch, P. A., et al. 2012, *ApJ*, 754, 83
- Bouwens, R. J., Illingworth, G. D., Oesch, P. A., et al. 2012, *ApJ*, 752, L5
- Calzetti, D., Armus, L., Bohlin, R. C., et al. 2000, *ApJ*, 533, 682
- Curtis-Lake, E., McLure, R. J., Dunlop, J. S., et al. 2012, *arXiv:1207.2727*
- Davé, R., Oppenheimer, B. D., & Finlator, K. 2011, *MNRAS*, 415, 11
- Davé, R., Finlator, K., & Oppenheimer, B. D. 2012, *MNRAS*, 421, 98
- de Barros, S., Schaerer, D., & Stark, D. P. 2012, *arXiv:1207.3663*
- Dekel, A., Birnboim, Y., Engel, G., et al. 2009, *Nature*, 457, 451
- Dutton, A. A., van den Bosch, F. C., & Dekel, A. 2010, *MNRAS*, 405, 1690
- Egami, E., Kneib, J.-P., Rieke, G. H., et al. 2005, *ApJ*, 618, L5
- Erb, D. K., Steidel, C. C., Shapley, A. E., et al. 2006, *ApJ*, 647, 128
- Erb, D. K., Pettini, M., Shapley, A. E., et al. 2010, *ApJ*, 719, 1168
- Eyles, L. P., Bunker, A. J., Stanway, E. R., et al. 2005, *MNRAS*, 364, 443
- Eyles, L. P., Bunker, A. J., Ellis, R. S., et al. 2007, *MNRAS*, 374, 910
- Faber, S. M., Phillips, A. C., Kibrick, R. I., et al. 2003, *Proc. SPIE*, 4841, 1657
- Finkelstein, S. L., Papovich, C., Salmon, B., et al. 2011, *arXiv:1110.3785*
- Finlator, K., Oppenheimer, B. D., & Davé, R. 2011, *MNRAS*, 410, 1703
- Förster Schreiber, N. M., Genzel, R., Bouché, N., et al. 2009, *ApJ*, 706, 1364
- Fumagalli, M., Patel, S., Franx, M., et al. 2012, submitted to *ApJ*, *arXiv:1206.2645*
- Giavalisco, M., Ferguson, H. C., Koekemoer, A. M., et al. 2004, *ApJ*, 600, L93
- Gnedin, N. Y., Tassis, K., & Kravtsov, A. V. 2009, *ApJ*, 697, 55
- González, V., Labbé, I., Bouwens, R. J., et al. 2010, *ApJ*, 713, 115
- González, V., Labbé, I., Bouwens, R. J., et al. 2011, *ApJ*, 735, L34
- González, V., Bouwens, R., Labbe, I., et al. 2011, *arXiv:1110.6441*
- Gordon, K. D., & Clayton, G. C. 1998, *ApJ*, 500, 816
- Grazian, A., Fontana, A., de Santis, C., et al. 2006, *A&A*, 449, 951
- Grogin, N. A., Kocevski, D. D., Faber, S. M., et al. 2011, *ApJS*, 197, 35
- Hainline, K. N., Shapley, A. E., Kornei, K. A., et al. 2009, *ApJ*, 701, 52
- Kennicutt, R. C., Jr. 1998, *ARA&A*, 36, 189
- Koekemoer, A. M., Faber, S. M., Ferguson, H. C., et al. 2011, *ApJS*, 197, 36
- Krumholz, M. R., & Dekel, A. 2012, *ApJ*, 753, 16
- Kuhlen, M., & Faucher-Giguère, C.-A. 2012, *MNRAS*, 423, 862
- Labbé, I., Bouwens, R., Illingworth, G. D., & Franx, M. 2006, *ApJ*, 649, L67
- Labbé, I., González, V., Bouwens, R. J., et al. 2010, *ApJ*, 708, L26
- Labbé, I., González, V., Bouwens, R. J., et al. 2010, *ApJ*, 716, L103
- Lee, J. C., Kennicutt, R. C., Funes, S. J., José G., Sakai, S., & Akiyama, S. 2007, *ApJ*, 671, L113
- Lee, K.-S., Ferguson, H. C., Wiklind, T., et al. 2012, *ApJ*, 752, 66
- Ly, C., Lee, J. C., Dale, D. A., et al. 2011, *ApJ*, 726, 109
- Maiolino, R., Nagao, T., Grazian, A., et al. 2008, *A&A*, 488, 463
- Mancini, C., Förster Schreiber, N. M., Renzini, A., et al. 2011, *ApJ*, 743, 86
- McLure, R. J., Dunlop, J. S., de Ravel, L., et al. 2011, *MNRAS*, 418, 2074
- Meurer, G. R., Heckman, T. M., & Calzetti, D. 1999, *ApJ*, 521, 64
- Narayanan, D., & Davé, R. 2012, *MNRAS*, 423, 3601
- Neistein, E., & Dekel, A. 2008, *MNRAS*, 383, 615
- Oke, J. B., & Gunn, J. E. 1983, *ApJ*, 266, 713
- Ono, Y., Ouchi, M., Shimasaku, K., et al. 2010, *ApJ*, 724, 1524
- Onodera, M., Arimoto, N., Daddi, E., et al. 2010, *ApJ*, 715, 385
- Osterbrock, D. E., & Ferland, G. J. 2006, *Astrophysics of gaseous nebulae and active galactic nuclei*, 2nd. ed. by D.E. Osterbrock and G.J. Ferland. Sausalito, CA: University Science Books, 2006,
- Papovich, C., Finkelstein, S. L., Ferguson, H. C., Lotz, J. M., & Giavalisco, M. 2011, *MNRAS*, 412, 1123
- Reddy, N. A., Erb, D. K., Pettini, M., Steidel, C. C., & Shapley, A. E. 2010, *ApJ*, 712, 1070
- Reddy, N. A., Pettini, M., Steidel, C. C., et al. 2012, *ApJ*, 754, 25
- Reddy, N., Dickinson, M., Elbaz, D., et al. 2012, *ApJ*, 744, 154
- Retzlaff, J., Rosati, P., Dickinson, M., et al. 2010, *A&A*, 511, A50
- Richard, J., Jones, T., Ellis, R., et al. 2011, *MNRAS*, 413, 643
- Richard, J., Kneib, J.-P., Ebeling, H., et al. 2011, *MNRAS*, 414, L31
- Robertson, B. E., & Kravtsov, A. V. 2008, *ApJ*, 680, 1083
- Robertson, B. E., Ellis, R. S., Dunlop, J. S., McLure, R. J., & Stark, D. P. 2010, *Nature*, 468, 49
- Salpeter, E. E. 1955, *ApJ*, 121, 161
- Santini, P., Fontana, A., Grazian, A., et al. 2009, *A&A*, 504, 751
- Schaerer, D., & de Barros, S. 2009, *A&A*, 502, 423
- Schaerer, D., & de Barros, S. 2010, *A&A*, 515, A73
- Shapley, A. E. 2011, *ARA&A*, 49, 525
- Schenker, M. A., Stark, D. P., Ellis, R. S., et al. 2012, *ApJ*, 744, 179
- Shim, H., Chary, R.-R., Dickinson, M., et al. 2011, *ApJ*, 738, 69
- Siana, B., Teplitz, H. I., Chary, R.-R., Colbert, J., & Frayer, D. T. 2008, *ApJ*, 689, 59
- Stark, D. P., Bunker, A. J., Ellis, R. S., Eyles, L. P., & Lacy, M. 2007, *ApJ*, 659, 84
- Stark, D. P., Ellis, R. S., Bunker, A., et al. 2009, *ApJ*, 697, 1493
- Stark, D. P., Ellis, R. S., Chiu, K., Ouchi, M., & Bunker, A. 2010, *MNRAS*, 408, 1628
- Stark, D. P., Ellis, R. S., & Ouchi, M. 2011, *ApJ*, 728, L2
- Trenti, M., Smith, B. D., Hallman, E. J., Skillman, S. W., & Shull, J. M. 2010, *ApJ*, 711, 1198
- Trump, J. R., Weiner, B. J., Scarlata, C., et al. 2011, *ApJ*, 743, 144
- Vanzella, E., Giavalisco, M., Dickinson, M., et al. 2009, *ApJ*, 695, 1163
- Wang, W.-H., Cowie, L. L., Barger, A. J., Keenan, R. C., & Ting, H.-C. 2010, *ApJS*, 187, 251
- Weinmann, S. M., Neistein, E., & Dekel, A. 2011, *MNRAS*, 417, 2737
- Windhorst, R. A., Cohen, S. H., Hathi, N. P., et al. 2011, *ApJS*, 193, 27
- Wuyts, S., Förster Schreiber, N. M., Lutz, D., et al. 2011, *ApJ*, 738, 106
- Zheng, W., Postman, M., Zitrin, A., et al. 2012, *arXiv:1204.2305*

TABLE 1  
GOODS BRIGHT 3.8  $< z < 5.0$  SPECTROSCOPIC SAMPLE

ID	RA(J2000)	DEC(J2000)	$z_{\text{spec}}$	$z_{850}$	$\Delta[3.6]$
S44_1649	03:32:05.022	-27:46:12.65	3.91	24.47	0.07
S43_2212	03:32:06.615	-27:47:47.69	3.94	24.28	0.13
S33_6294	03:32:14.497	-27:49:32.69	4.74	25.40	0.26
S33_8715	03:32:18.257	-27:48:02.53	4.28	24.65	0.45
S33_15763	03:32:27.939	-27:46:18.57	4.00	25.23	0.17
S23_20730	03:32:34.349	-27:48:55.81	4.14	24.11	0.22
S24_23979	03:32:38.729	-27:44:13.34	4.00	24.81	0.00
S23_24940	03:32:40.086	-27:49:01.21	4.13	26.45	0.35
S24_25118	03:32:40.385	-27:44:31.00	4.13	25.24	0.04
S22_25614	03:32:41.159	-27:51:01.50	4.06	25.25	0.42
S23_28451	03:32:46.247	-27:48:46.99	4.02	24.88	0.39
S12_29436	03:32:48.244	-27:51:36.90	4.36	24.87	0.67
S13_31908	03:32:54.035	-27:50:00.81	4.43	25.07	-0.25
S12_32366	03:32:55.249	-27:50:22.46	4.17	24.42	0.20
S12_33166	03:32:58.380	-27:53:39.58	4.40	25.75	0.14
S43_1669	03:32:05.080	-27:46:56.52	4.82	23.79	0.14
S44_1745	03:32:05.259	-27:43:00.42	4.80	25.24	0.14
S45_3792	03:32:10.027	-27:41:32.65	4.81	25.03	0.27
S34_11180	03:32:21.931	-27:45:33.07	4.79	25.82	0.17
S33_11861	03:32:22.884	-27:47:27.57	4.44	24.93	0.43
S33_11915	03:32:22.971	-27:46:29.08	4.50	25.34	0.33
S35_16226	03:32:28.563	-27:40:55.74	4.60	25.44	0.24
S31_16819	03:32:29.291	-27:56:19.46	4.76	25.05	0.10
S22_20041	03:32:33.475	-27:50:30.00	4.90	25.77	0.25
S24_24961	03:32:40.118	-27:45:35.47	4.77	25.55	0.45
S21_26522	03:32:42.623	-27:54:28.95	4.40	25.61	0.58
S12_32900	03:32:57.169	-27:51:45.01	4.76	24.64	0.40
N33_14884	12:36:42.235	+62:15:22.93	4.42	24.47	0.27
N14_27206	12:37:57.510	+62:17:18.77	4.71	23.82	0.28
N42_5352	12:36:14.513	+62:11:40.61	4.15	25.31	0.30
N42_12760	12:36:36.823	+62:12:04.03	3.90	24.94	0.35
N33_20202	12:36:55.940	+62:14:12.44	3.91	23.78	0.15
N33_25472	12:37:09.840	+62:14:39.37	4.25	25.01	0.32
N23_28987	12:37:19.688	+62:15:42.46	4.53	25.49	0.27
N34_21578	12:36:59.377	+62:19:05.41	3.86	25.30	0.10
N34_21756	12:36:59.758	+62:18:54.33	3.86	24.78	0.27
N34_23754	12:37:05.013	+62:17:31.01	3.93	24.62	0.31
N35_26133	12:37:11.814	+62:22:12.30	4.05	24.25	0.27
N35_26600	12:37:13.037	+62:21:11.16	4.05	24.09	0.33
N24_28740	12:37:19.003	+62:19:53.51	4.19	24.38	0.18
N25_29248	12:37:20.446	+62:22:14.85	4.05	24.63	0.58
N24_29391	12:37:20.845	+62:18:43.22	4.07	25.42	0.41
N32_22884	12:37:02.520	+62:11:55.00	4.02	25.64	0.10
N24_27374	12:37:15.103	+62:20:05.21	4.06	25.85	0.35
N42_8958	12:36:25.972	+62:08:59.43	4.14	24.36	0.49